Journal of Materials Chemistry C

ROYAL SOCIETY OF CHEMISTRY

REVIEW

View Article Online
View Journal | View Issue

Cite this: J. Mater. Chem. C, 2025, 13, 4836

X-ray luminescent metal–organic frameworks: design strategies and functional applications

Yuan Liang,[a] Jun-Zhe Zhu,[a] Sheng-Yu Jin,[a] Ya-Ru Meng,[a] Shu-Fan Li,[a] Jing-Lin Zuo, *[b] Gen Zhang *[a] and Jian Su*[ab]

X-ray scintillator materials have attracted considerable attention due to their versatile and remarkable properties, leading to advanced applications in materials science, information technology, and biomedicine. In this review, we carefully summarize the latest developments in metal–organic framework (MOF)-based X-ray scintillator materials. First, we discuss the design strategies for MOF-based X-ray scintillators from three perspectives: regulation of the inorganic and organic components, post-synthetic modification of frameworks, and guest-loading within MOF pores. Notably, many of these strategies, which have proven effective in enhancing the performance of other functional MOFs, have yet to be fully utilized to improve MOF-based X-ray scintillators. Second, among the reviewed MOF materials, we categorize them according to the position of the metal ions in the periodic table: fourth-period, fifth-period, and sixth-period metal elements. Within each category, we analyze the progress made with MOFs containing the same metal ion and explore the possible mechanisms behind their performance. Third, we highlight the applications of MOF-based X-ray scintillators in high-sensitivity and high-resolution X-ray detectors, flexible imaging, and X-ray radiation therapy. In this section, we aim to elucidate the relationship between the structural characteristics of MOFs and their practical applications. Finally, based on the achievements discussed, we provide insights into the limitations, major challenges, and future directions in this area, with the hope of inspiring further research on MOF-based X-ray scintillators and their advanced applications. We aspire that this review will encourage innovative research leading to the development of smarter fluorescent materials and devices.

Received 16th December 2024,
Accepted 22nd January 2025

DOI: 10.1039/d4tc05299d

rsc.li/materials-c

1. Introduction

Scintillators belong to a category of functional materials that are capable of emitting visible light upon excitation by high-energy radiation, such as X-rays.[1–4] These materials are crucial for radiation detection and measurement in areas such as nuclear activities, high-energy physics research, homeland security and medicine.[5–9] Improving the chemical stability and biocompatibility of scintillators is the focus of current research to ensure they can be safely used in medical imaging and therapy. With the increasing concern about the environmental impact, researchers are looking for environmentally friendly X-ray scintillator materials. Generally, based on the constitutions, scintillators are mainly divided into inorganic scintillators and organic scintillators. Inorganic scintillators have been around since 1895,[10] while organic scintillators were first reported in 1947.[11] Inorganic scintillator materials offer many traditional advantages, such as their typically high light yields and excellent energy resolution, but they are often brittle and prone to breakage during processing or use. Especially for large-sized and high-purity inorganic crystals, the production cost may be high.[12] Organic scintillator materials offer significant advantages in terms of material preparation, property tuning, and large-area preparation, but they typically have weak absorption of X-rays, resulting in low radioluminescence (RL) efficiency.[13] Organic materials may be less stable when exposed to radiation over a long period of time and less resistant to radiation than inorganic materials.[14] Although existing X-ray scintillator materials perform well in some applications, they still have limitations such as brittleness, sensitivity to environmental conditions, high cost, and difficulty in mass production. To overcome these limitations, inorganic–organic hybrid materials have emerged. They combine the structural diversity, high quantum efficiency, and good optical properties of inorganic materials with the advantages of low cost, flexibility, and tunable optical properties of organic materials.[15,16] Inorganic–organic hybrid materials, through the synergistic integration of

[a] School of Chemistry and Chemical Engineering, Nanjing University of Science and Technology, Nanjing, 210094, P. R. China. E-mail: zhanggen@njust.edu.cn, sujian@njust.edu.cn
[b] State Key Laboratory of Coordination Chemistry, School of Chemistry and Chemical Engineering, Nanjing University, Nanjing 210023, P. R. China. E-mail: zuojl@nju.edu.cn

inorganic and organic components, exhibit novel properties, including high carrier transport capacity and enhanced light absorption capability. Because of these characteristics, inorganic–organic hybrid materials show significant potential and application prospects in the field of X-ray scintillators.[17,18]

Among the diverse inorganic–organic hybrid materials, metal–organic frameworks (MOFs) are a kind of porous crystalline materials formed by the connection of metal ions/clusters with organic linkers through coordination bonds. By changing the type of metal ion or organic ligand, the physical and chemical properties of MOFs can be precisely regulated to achieve optimization for specific applications.[19–21] For instance, Qian *et al.* have meticulously summarized the design and construction of various luminescent functional MOFs.[22,23] Furthermore, the porosity of MOFs has demonstrated its advantages in fields such as gas adsorption/separation,[24] catalysis,[25] and energy transformation.[26] Although high porosity in MOFs results in low density, which tends to reduce scintillation performance, it nonetheless provides an additional dimension of MOF decoration through host–guest chemistry. Notably, filling the cavities with appropriate functional guest molecules can not only decrease the porosity of MOFs but also potentially enhance their luminescent and radiation-responsive efficiencies.[27] By selecting different high ordinal number metal atoms, designing specific organic ligands, and adopting appropriate post-synthetic modification strategy, the X-ray absorption efficiency, luminescent wavelength and intensity of MOFs can be adjusted to suit different application requirements.[27–30] Future research may focus on developing MOFs with novel structures to improve X-ray absorption and luminescent efficiency. The luminescent characteristics of MOFs are further optimized to meet the needs of high-speed imaging and biomedicine of scintillators.[27,28] In addition, research will focus on how to further enhance the performance through nanotechnology, composite material design and interface engineering.

Recently, the fundamental mechanisms of X-ray scintillation using MOFs have been comprehensively reviewed in two recently published works.[27,28] Therefore, those discussions will not be included here. In this review, we summarize the development of MOF-based X-ray scintillators with different periodic elements and highlight their unique advantages. Additionally, we clearly present the existing applications of these scintillator materials. Ultimately, we offer an analysis of the limitations, major challenges, and future opportunities of MOF-based X-ray scintillators. We aspire for this comprehensive analysis to stimulate groundbreaking studies focused on enhancing the utilization of novel MOF-based scintillators, thereby fostering progress in the realms of X-ray visualization and intelligent material technologies.

2. Design strategies of MOF-based X-ray scintillators

The targeted design of MOF-based scintillators is a highly specialized and multidisciplinary field, which involves many disciplines such as materials science, chemistry, physics and engineering. The goal of directional design is to create MOFs with specific performance to meet the specific needs of X-ray scintillator applications. Herein, we will propose several strategies related to the advances of coordination chemistry (Fig. 1).

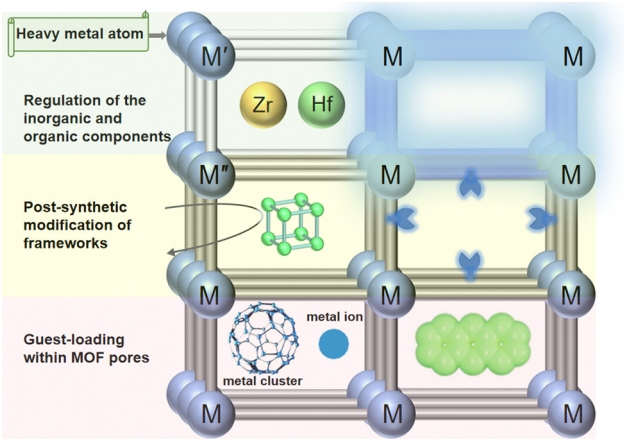

Fig. 1 Design strategies of MOF-based X-ray scintillators.

2.1. Regulation of the inorganic and organic components

In the design of the pristine MOFs, one of the strategies was to assemble with heavy metal elements with higher atomic numbers (such as Zr, Hf, U, *etc.*),[31,32] which possess distinct help to improve the absorption capacity of MOFs to high-energy radiation.[33,34] For instance, Yin *et al.* used the red, green, and blue luminescent properties of Eu^{3+}, Tb^{3+}, and Dy^{3+}, combined with the principle of three primary colors, to prepare mixed metals with white light emission at 275 nm excitation.[35] Another strategy involves decorating coordination groups with luminescent organic units (such as anthracene, naphthalene, coumarin derivatives, *etc.*). By linking these units with heavy metal nodes, they can function not only as bridging ligands to enhance the optical properties of MOFs, but also play an important role in applications such as photocatalysis or sensing.[33,34] For example, Yang *et al.* regulated the energy transfer efficiency of ligands to europium ions by introducing boric acid groups on terephthalic acid, and constructed multi-luminescent MOFs by using ligands and metal ions to emit light at the same time.[36]

2.2. Post-synthetic modification of frameworks

Framework modification is a method to optimize the performance of an MOF skeleton by changing its metal nodes or ligands. This strategy can significantly affect the chemical and physical properties of MOFs, thereby expanding their applications in different fields. On the one hand, replacement and introduction metal ions in the metal nodes, can change the electronic structure and optical properties of the pristine MOFs.[37,38] Replacing Cd ions with Co ions, for example, may introduce new electronic properties that improve the performance of MOFs in specific chemical reactions.[39–41] On the other hand, covalent modification with ligands can alter their

chemical stability, pore environment, and optical response.[42] For example, the introduction of tetraphenylvinyl groups in MOFs enables a transition from non-fluorescent to fluorescent through specific chemical modifications.[43]

2.3. Guest-loading within MOF pores

Guest-loading is a strategy by introducing additional molecules or ions into the channel of an MOF. Such loads can be heavy metal ions/clusters, organic luminescent units, or other functional molecules designed to improve the performance of MOFs in specific applications. Loading of heavy metal ions/clusters, can enhance the absorption capacity of MOFs to X-rays or other forms of radiation, thereby improving their performance as scintillators.[44] For example, the adsorption capacity of MOFs to water vapor and heavy metal ions was studied in recent years.[45] MOFs have demonstrated efficacy as adsorbents for heavy metal ions, attributable to their expansive surface area and customizable pore dimensions.[46,47] Loading of organic luminescent molecules (such as fluorescent dyes, phosphorescent dyes) can enhance the optical properties of MOFs, making it have better application prospects in sensing and imaging fields. For example, Qian *et al.* innovatively proposed the idea of using ion exchange method to assemble organic laser dye molecules into one-dimensional pores of MOFs to prepare micron-scale two-photon pump laser media, and successfully realized two-photon pump luminescent and laser emission in solid state.[48]

Actually, the directional design of MOF scintillator is a complex process, which requires comprehensive consideration of many factors. With advances in material synthesis technology and the development of computational simulation tools, future MOF scintillator designs will be more accurate and efficient, able to meet the stringent requirements of specific applications.

3. Classification of different types of MOF-based X-ray scintillators

There are many kinds of MOF-based X-ray scintillation. Herein, we divided these MOFs into three categories according to heavy metal atom substitution: fourth, fifth and sixth cycle. In this review, we will summarize and discuss common MOF-based scintillator materials through specific examples.

3.1. MOFs with fourth period metal element

3.1.1. Cu cluster-based MOFs. Inorganic materials containing copper are commonly used as X-ray scintillators.[34] The solvothermal synthesis of $Cu_6S_6L_6$ (L = 4,6-dimethylpyrimidine-2-thione) shows a high photoluminescence quantum yield (PLQY) of 54.5% and an X-ray yield of 3721 photons/MeV.[49] The scintillation screen prepared by homogeneous dispersion of lead-free perovskite nanoparticles ($Cs_3Cu_2I_5$) in styrene monomer achieves a high quantum yield of 87.2%, a spatial resolution of 7.3 lp mm^{-1}, a low detection limit of 63 nGy_{air} s^{-1}, and excellent radiation stability.[50] These advances highlight the important role of copper-based materials in enabling efficient, high-resolution X-ray imaging. However, there is nearly no report on Cu-MOF as X-ray scintillators. The d^{10} electron configuration of Cu(I) ion and Cu(I) clusters is beneficial for achieving most of thermally activated delayed fluorescence (TADF) or other luminescent, which may allow them to fluoresce under X-ray excitation. Notably, Cu(I) clusters can increase the abundance of Cu elements, and the aggregate of copper atoms may enhance the capacity of light absorption and charge transport. Meanwhile, the inorganic heavy element iodine existed in the CuI clusters,

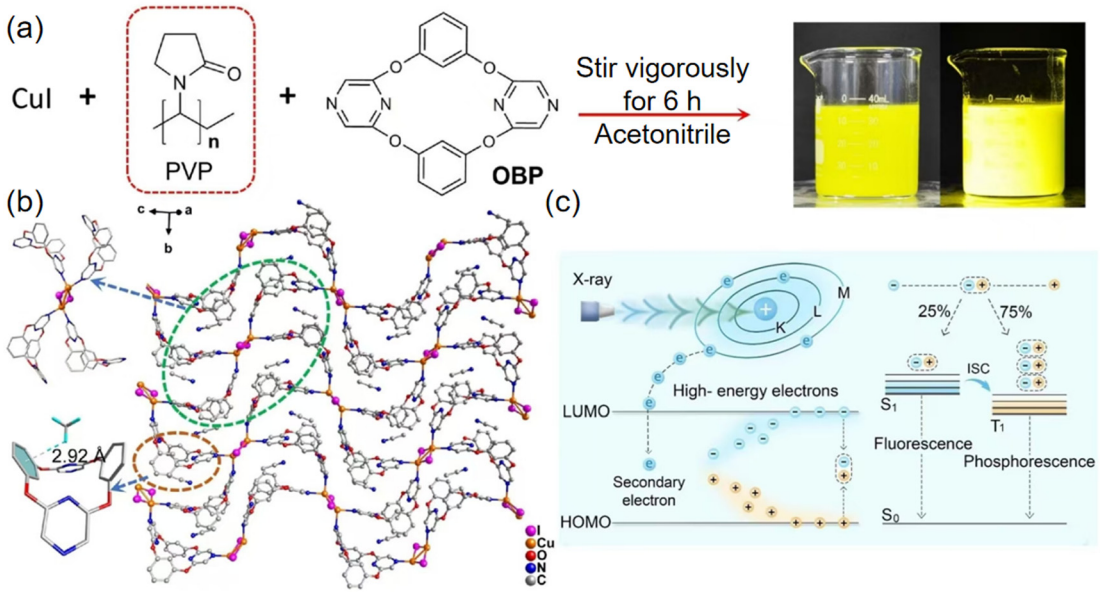

Fig. 2 (a) The preparation method of **Cu-MOF 1-rod**. (b) Crystal structure of **Cu-MOF 1**. (c) Scintillation mechanism of the detector. Reprinted with permission.[51] Copyright 2023, Wiley.

which further enhanced the X-ray absorption and improved the luminescent performance. For instance, in 2023, Peng *et al.* constructed a copper iodide cluster-based MOF scintillator (**Cu-MOF 1**) (Fig. 2b) using the aggregation-induced emission (AIE)-activated oxacalix-[2]benzene-[2]pyrazine (OBP) as an organic linker.[51] The introduction of macrocycle AIE bridging ligand, coupled with the compact framework structure, endows **Cu-MOF 1** with high X-ray excited luminescence (XEL) efficiency and excellent chemical stability. Furthermore, the OBP ligand and copper iodide were integrated within PVP micelles, yielding microcrystals that exhibit a uniform rod-like shape (**Cu-MOF 1-rod**) (Fig. 2a). The XEL mechanism of **Cu-MOF 1** is depicted in Fig. 2c: When subjected to the stimulation of energetic ionizing radiation, the scintillating material captures X-ray photons, leading to the ejection of energetic electrons *via* photoelectric effect and Compton scattering. These electrons trigger a chain reaction of secondary electrons by impacting nearby atoms, creating additional electrons and holes. Following this, the electrons and holes combine to create excitons. Ultimately, these excitons revert to their ground state (S_0) *via* an emission of light, manifesting as visible fluorescence or phosphorescence. This microcrystalline scintillator, **Cu-MOF 1-rod**, was crafted into a screen with exceptional flexibility and stability, suitable for high-quality X-ray imaging even under conditions of extreme humidity.

More recently, Alexander V. Artem'ev *et al.* have developed a remarkable array of CuI-based 1D coordination polymers (CPs) (**3**, **7**) (Fig. 3c and d), using diverse 2-alkylsulfonylpyridines as 1,3-*N*,*S*-ligands (Fig. 3a and b).[52] The registered RL spectra (Fig. 3e) closely match the PL spectra, suggesting identical emission states for both phenomena. In general, the detected RL intensity is roughly in line with the PLQYs across the samples. CP **3** stands out as an exceptionally efficient RL

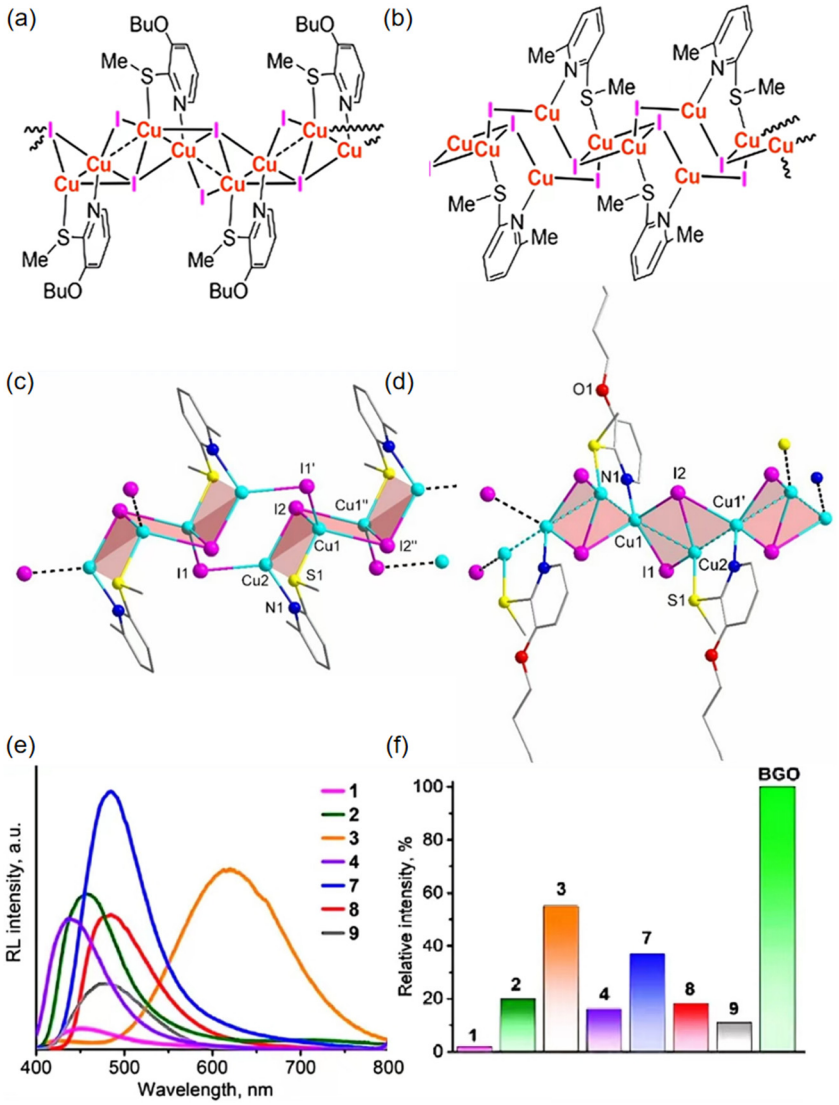

Fig. 3 Molecular structures of **1** (a) and **3** (b). 1D chain-like structures of **3** (c) and **7** (d) (296 K, without H atoms). (e) RL spectra of **1–4** and **7–9** at 298 K. (f) RL intensities of **1–4** and **7–9** to those of BGO, under the same dose rate (298 K). Reprinted with permission.[52] Copyright 2023, Royal Society of Chemistry.

emitter, characterized by both an intense and broad emission line. The luminescent efficiency of CP **3** can reach to 55% when compared to the benchmark scintillator $Bi_4Ge_4O_{12}$ (BGO), as illustrated in Fig. 3f. Under ambient conditions, these CPs unusually possess a short PL lifetime, specifically within the range of 0.4 to 2.0 μs. Even though there has been no further detailed study of the performance of these scintillators, this work demonstrates the potential for coordination polymers to be finely tuned in order to meet the requirements of functional scintillators.

3.1.2. Ca-MOF. Ca^{2+} typically forms a stable coordination environment, which may endow Ca-MOFs with good thermal and chemical stability under various conditions. By altering the organic ligands and synthesis conditions, the pore size and porosity of Ca-MOFs can be tailored, a feature that is crucial for applications such as gas storage/separation and catalysis. The chemical composition and structure of Ca-MOFs can be designed to achieve specific functions by selecting different organic ligands and employing various synthesis strategies. For instance, in 2019, Lu *et al.* selected polycyclic aromatics 5-[(anthracen-9-ylmethyl)-amino]-isophthalic acid (H_2L^1) and 5-[(pyren-1-ylmethyl)-amino]-isophthalic acid (H_2L^2), in conjunction with $Ca(NO_3)_2{\cdot}4H_2O$, to create two distinct MOFs: $[Ca_2(L^1)_2(DMF)_2(H_2O)]_n$ (**Ca-SMOF 1**) (Fig. 4a) and $[Ca_2(L^2)_2(DMF)_2]_n{\cdot}0.5nH_2O$ (**Ca-SMOF 2**) (Fig. 4b).[53] Upon exposure to cathode rays, both **Ca-SMOFs 1–2** demonstrated significant cathode-ray luminescence (CL) scintillation. To elucidate the scintillating characteristics triggered by ionizing radiation, the powdered forms of **Ca-SMOF 1** and **Ca-SMOF 2** were introduced into the detection apparatus to gather CL luminescent signals at ambient temperature. Under a high-vacuum environment and exposed to energetic electron beams emitted by a 20 keV electron source, **Ca-SMOF 1** and **Ca-SMOF 2** each presented their unique CL signatures. **Ca-SMOF 1** emits a peak at approximately 478 nm, whereas peak of **Ca-SMOF 2** located at approximately 442 nm (Fig. 4c and d). In addition to the intense emission, **Ca-SMOF 1** also displays supplementary CL bands ranging from 320 to 380 nm and 260 to 290 nm. **Ca-SMOF 2**, akin to **Ca-SMOF 1**, presents additional emission peaks between 330 and 360 nm and 260 to 280 nm. The experimental CL spectra data reveal that **Ca-SMOFs 1–2**, composed of π-conjugated luminescent units and calcium ions, exhibit a vigorous response to cathode-ray-induced ionization through cooperative effects.

Even though numerous Cu-clusters have been thoroughly examined in the field of scintillators,[51,54] there are only a limited number of examples of MOFs constructed using fourth-cycle transition metals that exhibit superior performance. Despite the relatively low atomic number of these fourth-cycle transition metals, which is not conducive to X-ray absorption, their coordination behavior holds potential for the construction of related MOF-based scintillators. For instance, the coordination between

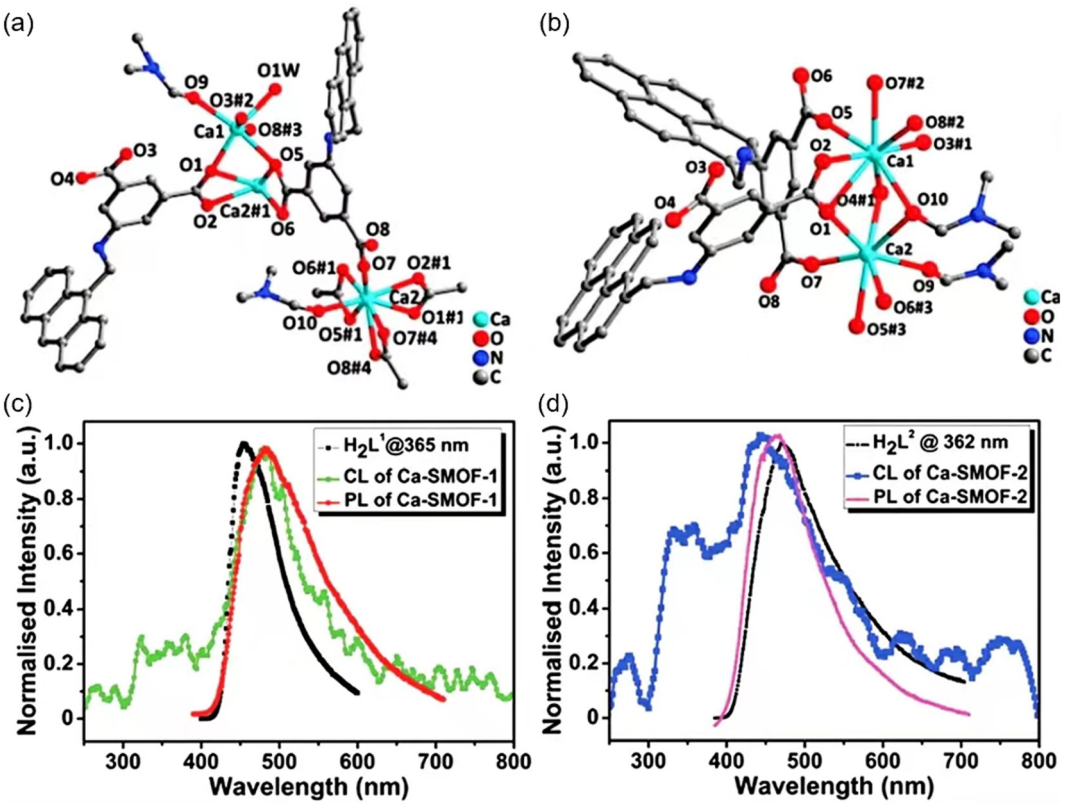

Fig. 4 The coordination configuration of Ca1 and Ca2 for **Ca-SMOF 1** (a) and **Ca-SMOF 2** (b). The CL and PL spectra of **Ca-SMOF 1** (c) and **Ca-SMOF 2** (d), along with the spectra of their respective free ligands, H_2L^1 and H_2L^2. Reprinted with permission.[53] Copyright 2019, Royal Society of Chemistry.

Cu(I) and the iodine element from the fifth period is particularly beneficial for X-ray absorption. In summary, numerous elements within this cycle remain unstudied, indicating vast opportunities for the development of 3d metal-based MOFs in the X-ray field.

3.2. MOFs with fifth period metal element

The larger ionic radius of the fifth period elements enables them to coordinate with more ligands, resulting in high coordination numbers and a variety of coordination geometries, such as tetrahedral, octahedral, and square planar configurations. This structural diversity enriches the design of MOFs with diverse pore properties and functions. Furthermore, these elements can form complex structural models, including multi-nuclear metal clusters, which add to the functional complexity of MOFs. By fine-tuning the coordination environment, including the type of ligand and the charge on the metal center, the performance of MOFs can be optimized to cater to specific application requirements.

3.2.1. Zr-MOF. Zr-MOFs are renowned for their exceptional thermal and chemical stability, a critical attribute for X-ray imaging applications where equipment may be subjected to demanding conditions. Zr-MOFs possessed excelled stability and porosity, have attract widely attention in MOF materials. The utilization of meticulously designed Zr-MOFs spans across various domains such as catalysis, molecular adsorption and separation, drug delivery systems, fluorescence-based sensing, and the creation of porous carriers, among others.[55] Through precise self-assemble, Zr-MOF has shown great potential and application prospects in high-performance X-ray scintillators. For instance, in 2021, J. Perego *et al.* constructed the fluorescent

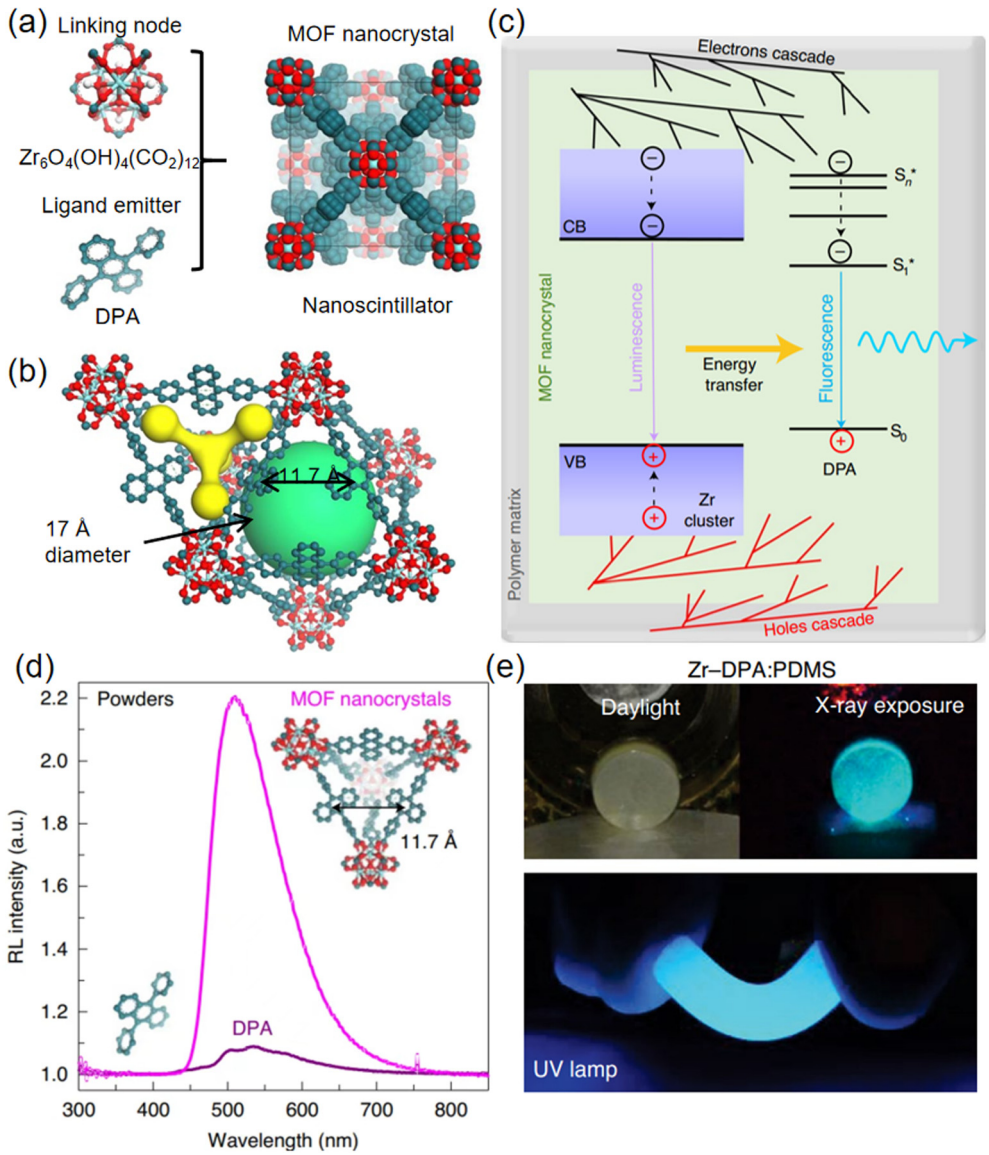

Fig. 5 (a) Crystal structure of **Zr-DPA**. (b) The tetrahedral and octahedral cavities present within the MOF frameworks. (c) Photophysical mechanisms that drive the scintillation effect. (d) RL spectra of MOF nanocrystals and DPA. (e) Pictures of the **Zr-DPA**: PMDS nanocomposite exposed to X-rays and UV light. Reprinted with permission.[56] Copyright 2021, Springer Nature.

MOF nanocrystals (**Zr-DPA**) (Fig. 5b) using the zirconium oxo-hydroxy clusters and the fluorophore linker dicarboxy-9,10-diphenylanthracene (DPA) (Fig. 5a).[56] DPA, known for its scintillating properties, serves as a ligand owing to its elevated fluorescence quantum yield of 0.96 and its distinct absorption and emission bands, which help to reduce the reabsorption of emitted light. To achieve a flexible material, transparent polydimethylsiloxane (PDMS) polymer was filled with high-Z fluorescent **Zr-DPA** nanoparticles. In this nanocomposite, ionizing radiation interacts with the polymer and MOF nanoparticles, producing free charges that, upon recombination, form luminescent singlet states on DPA molecules detectable by a photon detector. The matching of the X-ray-induced emission from the clusters with DPA absorption spectrum facilitates the sensitization of singlets *via* energy transfer, both radiatively and non-radiatively, from the excited clusters (Fig. 5c). Fig. 5d illustrates the RL spectrum of the nanocrystal powder in contrast to that of the unadulterated DPA powder under continuous X-ray excitation. The enhancement effect of the zirconium oxo-hydroxy clusters is apparent. This prototype demonstrates an exceedingly rapid scintillation response time of approximately 50 ps, marking it as a viable contender for advancing scintillator technology. These hybrid nanocomposites (Fig. 5e), hold promise as key elements in the development of flexible scintillating systems.

Another representative example in this domain was reported by Wang *et al.* in 2022. In their work, they constructed the **Zr-fcu-BADC-MOF** (D)-TADF chromophore (A) nanocomposite films (D–A_n) according to the methods illustrated in Fig. 6a.[57] The RL patterns of D–A_n nanocomposite films are closely parallel to those of the PL spectra, with a noticeable reduction

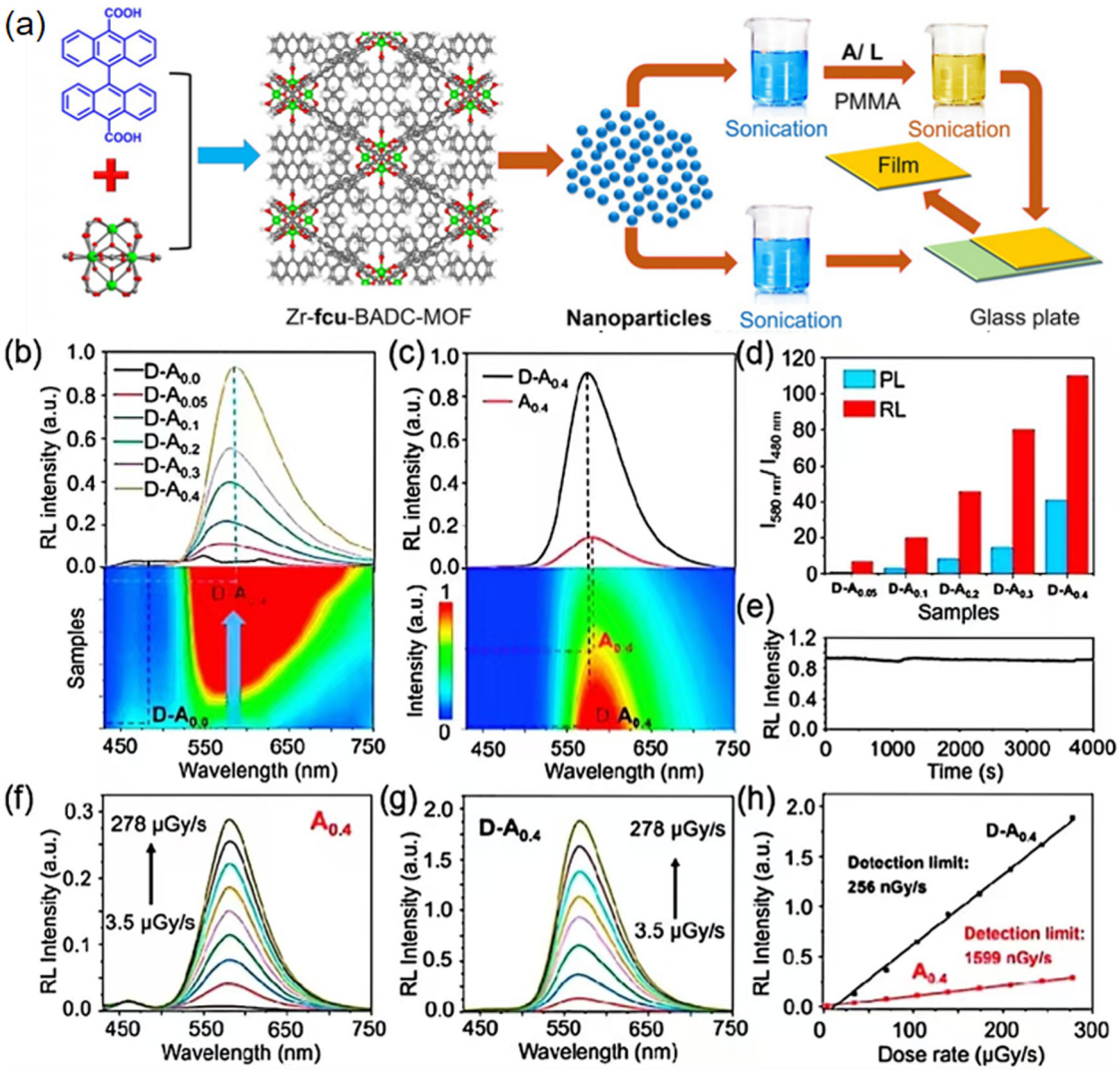

Fig. 6 (a) The synthesis routes for assembly of the **Zr-fcu-BADC-MOF** integrated with TADF chromophore nanocomposite films. (b) RL spectra of the D–A_n nanocomposite films. (c) RL spectra of the D–$A_{0.4}$ nanocomposite film and the $A_{0.4}$ film, under an X-ray dose rate of 174 mGy s^{-1}. (d) Ratios of emission intensity at 580 nm to that at 480 nm, triggered by UV and X-ray excitation, with $I_{580\,nm}/I_{480\,nm}$ indicating the intensities at the respective wavelengths. (e) RL intensity at 580 nm for the D–$A_{0.4}$ nanocomposite film, under continuous X-ray irradiation of at a dose rate of 174 mGy s^{-1}. The dose-rate-dependent RL spectra of both the $A_{0.4}$ film (f) and the D–$A_{0.4}$ nanocomposite film (g) are examined across a dose rate range of 3.5–278 mGy s^{-1}. (h) Detection thresholds of the D–$A_{0.4}$ nanocomposite film (black line) and A0.4 film (red line). Reprinted with permission.[57] Copyright 2021, Elsevier.

in RL intensity of the D film as component A is introduced (Fig. 6b). The RL intensity at the peak emission wavelengths of A is markedly boosted through energy transfer from the **Zr-fcu-BADC-MOF** (Fig. 6c). The total dampening of the **Zr-fcu-BADC-MOF** RL and the simultaneous increase in the RL of the TADF chromophores upon X-ray stimulation underscore the efficacy of the energy transfer process. The ratio of luminescent intensity at 580 nm to that at 480 nm, as measured by the RL, is roughly two to five times greater than the ratios achieved through ultraviolet light excitation. (Fig. 6d). Consequently, the immediate utilization of both singlet and triplet excitons for RL emission through the decay pathways of the TADF chromophores plays a substantial role in boosting the RL intensity. This is because a quarter of the excited states resulting from ion recombination post X-ray exposure are singlet states, while three-quarters are triplet states. Furthermore, the D–A nanocomposite film demonstrates excellent photostability, with the RL intensity sustaining approximately 98% of its original level under continuous ionizing radiation at a dose rate of 174 μGy s^{-1} over a period of 4000 s, rivaling the performance of commercial plastic scintillators (Fig. 6e). The XEL intensities of the $A_{0.4}$ film and D–$A_{0.4}$ nanocomposite film exhibit a direct linear relationship with the dose rate of the incident X-rays (Fig. 6f and g, respectively). The detection sensitivity has been markedly enhanced, decreasing from 15 000 nGy s^{-1} for the **Zr-fcu-BADC-MOF** film and 1600 nGy s^{-1} for the A film to 256 nGy s^{-1} for the D-$A_{0.4}$ nanocomposite film (Fig. 6h), which is roughly 22 times lower than the typical exposure rate for X-ray diagnostic procedures (5.5 μGy s^{-1}). This advancement in the efficiency of energy transfer at interfaces and the effective utilization of both singlet and triplet excitons from the TADF chromophore have resulted in a significant enhancement of RL upon X-ray irradiation. The engineered scintillator for X-ray imaging, boasting a detection threshold of 256 nGy s^{-1}, is roughly 22 times beneath the typical dosage used in medical diagnostics, making it an exemplary contender for applications in X-ray imaging. These findings present innovative design criteria for crafting scintillating materials that offer remarkably low detection thresholds coupled with enhanced imaging clarity.

More recently, Zhang *et al.* constructed a MOF **Y-PCN-94** scintillator using an AIEgen (4′,4″,4‴,4⁗-(ethene-1,1,2,2-tetrayl)-tetrakis([1,1′-biphenyl]-4-carboxylic acid), H_4ETTC) ligand (Fig. 7a–c).[58] The scintillation mechanism of this MOF involves a three-step process: To begin with, X-ray photons engage with zirconium clusters, prompting the expulsion of core electrons. Following this, a chain reaction generates a flurry of secondary electrons and electron–hole pairs through electron–electron interactions and Auger decay. Finally, the energy released from the union of these electron–hole duos stimulates the electron transition in the MOF, triggering the release of native PL when subjected to ultraviolet (UV) light (Fig. 7e). Upon exposure of

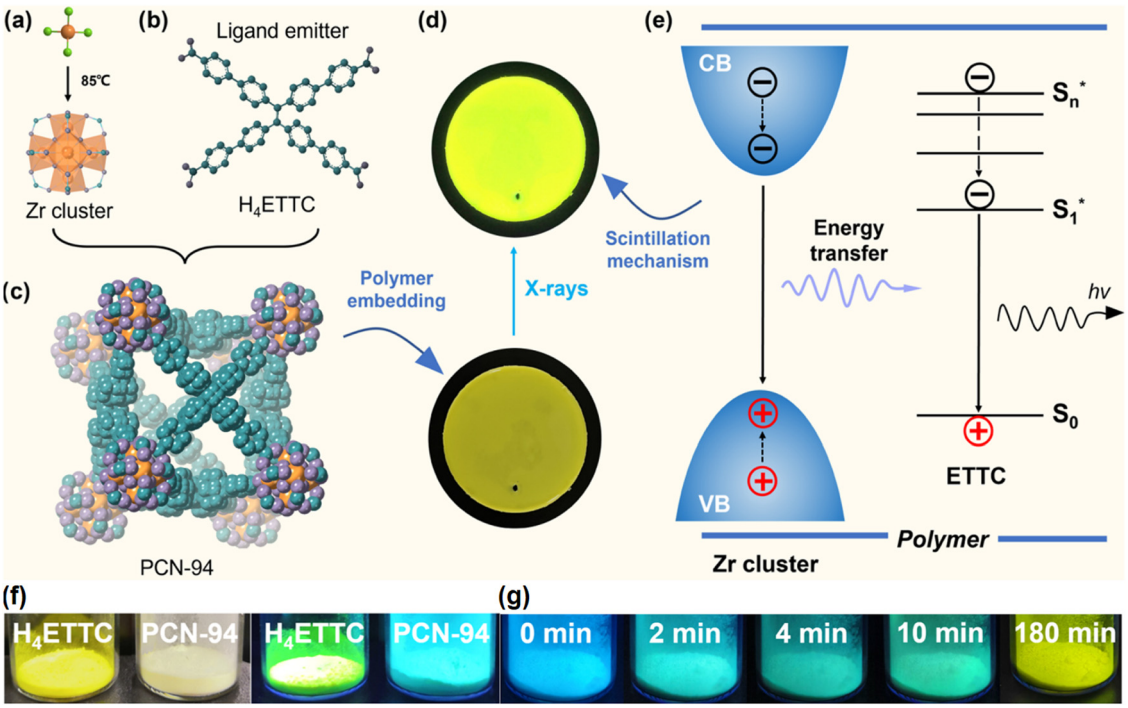

Fig. 7 (a) The synthesis of Zr-based clusters is initiated by the pre-assembly of $ZrCl_4$ at 85 °C. (b) Molecular structure of the organic ligand H_4ETTC. (c) Cystalline structure of **PCN-94** in a stacking model. (d) Photograph captures the composite scintillator membrane, which incorporates **PCN-94** nanocrystals within a polymer matrix, under X-ray exposure. (e) The fundamental scintillation process of the composite membrane. (f) Images of H_4ETTC and **PCN-94** are displayed under ambient light and UV light. (g) fluorescent images illustrate the transformation of **PCN-94** to **Y-PCN-94** after being exposed to air for varying durations, from 0 to 180 min, presenting the change process from **PCN-94** to **Y-PCN-94**. Reprinted with permission.[58] Copyright 2023, American Chemical Society.

PCN-94 to atmospheric conditions, there is a gradual transition in the emitted light from blue to yellow hues (Fig. 7g). The current study introduces an innovative approach to fabricating stable X-ray imaging materials by integrating AIE-active motifs into the framework structure, thereby enhancing the advancement of efficient MOF-based scintillator materials.

3.2.2. Sr-MOF. Strontium, an alkaline earth metal, boasts a larger ionic radius than Zr, a feature that could potentially endow Sr-MOFs with distinct skeleton structures. This architectural advantage might amplify the X-ray scattering cross-section, thereby enhancing the sensitivity of X-ray detection. Furthermore, the coordination geometry preferred by strontium, which often inclines towards an octahedral or polyhedral configuration, could introduce a variety of pore shapes and dimensions. This diversity contrasts with the typical tetrahedral coordination of Zr and may impact the efficiency of MOF in scattering and absorbing X-rays. In all, Sr-MOFs could provide unique structural and electronic properties that may improve X-ray detection capabilities, offering a complementary approach to material design in this field.

For instance, in 2023, Wang *et al.* constructed a 3D Sr-based SMOF $[Sr_2(DOBPDC)_2(DMF)]_n$ (**Sr-MOF**) using luminescent 3,3′-dihydroxy-4,4′-biphenyldicarboxylic acid ($H_2DOBPDC$) (Fig. 8a) ligand.[59] This MOF shows robust structure to resist light, heat and moisture. The scintillation mechanism of **Sr-MOF** is primarily attributed to the absorption of X-rays by the strontium atoms within the framework. This process facilitates the transfer of energy to the organic ligand, inducing an electronic transition to an excited state. Subsequently, the ligand returns to its ground state through a radiative transition, emitting fluorescence (Fig. 8b). In terms of X-ray scintillation properties, the Sr-MOF exhibited a characteristic blue emission peak at 430 nm under X-ray excitation. Its RL intensity increased continuously with the increasing X-ray dose rate, demonstrating an efficient X-ray response (Fig. 8c). Furthermore, the detection limit of the Sr-MOF was 4.96 μGy s^{-1} (Fig. 8d), which is slightly lower than the requirement for medical diagnosis (5.50 μGy s^{-1}), indicating its high sensitivity and potential application in X-ray detection.

MOFs constructed from fifth-period transition metals such as Zr and Sr have made significant research progress in the field of X-ray imaging and show great potential for future development. These materials leverage their high atomic number and highly efficient luminescent properties, making them excellent candidates for high-resolution X-ray imaging with superior image quality.[57,62] Despite the promising applications of fifth-period elements in MOFs, many of these elements remain inadequately explored. For instance, Ag^+, Cd^{2+}, and In^{3+} metal ions and their clusters are commonly employed as metal nodes in the construction of diverse structural and functional MOFs. Future research could concentrate on developing novel structures that leverage these

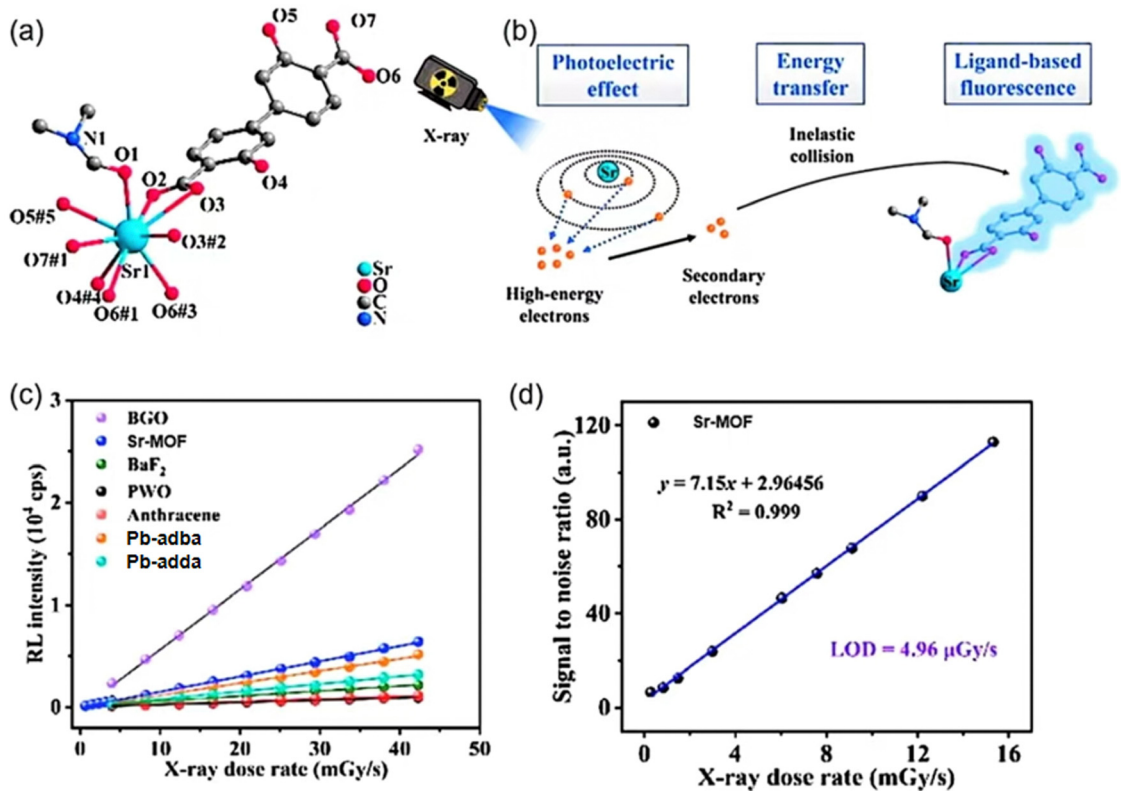

Fig. 8 (a) The coordination environment of Sr^{2+} centers in **Sr-MOF**. (b) Diagram of the RL mechanism of **Sr-MOF**. (c) The linear relationship between RL intensity and X-ray dose rates of **Sr-MOF**, BGO, PWO, BaF_2, organic crystal anthracene and reported Pb-based SMOFs (**Pb-adba**[60] and **Pb-adda**[61]). (d) The detection limit is Sr-MOF.[59] Copyright 2023, Royal Society of Chemistry. Reprinted with permission.[59]

metal elements to enhance X-ray absorption and luminescent efficiency.

3.3. MOFs with sixth period metal element

3.3.1. Hf-MOF. Normally, Hf-MOF possess similar structures of Zr-MOF. The higher atomic number of Hf enables Hf-MOF to potentially exhibit superior X-ray adsorption compared to Zr-MOF. These properties make Hf-MOF potentially advantageous in X-ray fluorescence imaging and other related applications. For instance, in 2014, Wang *et al.* created MOFs featuring high Z metal clusters $M_6(\mu_3\text{-}O)_4(\mu_3\text{-}OH)_4(\text{carboxylate})_{12}$ (M = Hf or Zr) (**Hf-DPA** and **Zr-DPA**) as connecting nodes and the 9,10-anthacenyl bis(benzoic acid) (DPA) as the bridging ligand (Fig. 9a).[62] The two MOFs possess the UiO structure of the fcu topology, which is achieved by bridging the $M_6(\mu_3\text{-}O)_4(\mu_3\text{-}OH)_4(\text{carboxylate})_{12}$ SBU to the linear L linkers (Fig. 9b). Notably, **Hf-DPA** and **Zr-DPA** exhibit notably extended lifetimes of 6.19 and 5.96 ns, respectively (Fig. 9c) contrasting with the 2.0 ns of solid DPA. This significant variation is presumably due to the interplay between solvent impact on the excited-state duration and the efficient transport of excitons among the compact DPA particles. The X-ray induced luminescence spectrum of these MOF samples, as determined with a specialized apparatus that includes an X-ray emitter, a monochromator, and an electron-multiplying charge-coupled device, displayed peaks between 400 to 600 nm (Fig. 9d and e), indicating the capability to transform X-ray energy into visible light. The MOF materials demonstrate high efficiency as X-ray scintillators, capitalizing on the synergistic effect of X-ray absorption by the metal cluster SBUs and optical emission by the bridging ligands. In view of the structural similarity between **Zr-DPA** and **Hf-DPA** and the extensive research on **Zr-DPA**, we can say that the existing research results obtained by **Zr-DPA** have not only laid a solid foundation for the future development of **Hf-DPA**, but also opened up diverse application prospects and research directions.

3.3.2. Pb-MOF. Lead glass for X-ray protection is a glass material containing a high proportion of lead, which can effectively shield X-rays and gamma rays and protect personnel from radiation damage. Despite containing a higher proportion of lead, Pb–glass can still maintain a certain degree of transparency and is suitable for occasions where protection and observation need to be considered at the same time. Perovskite materials are the most common X-ray scintillator materials, in

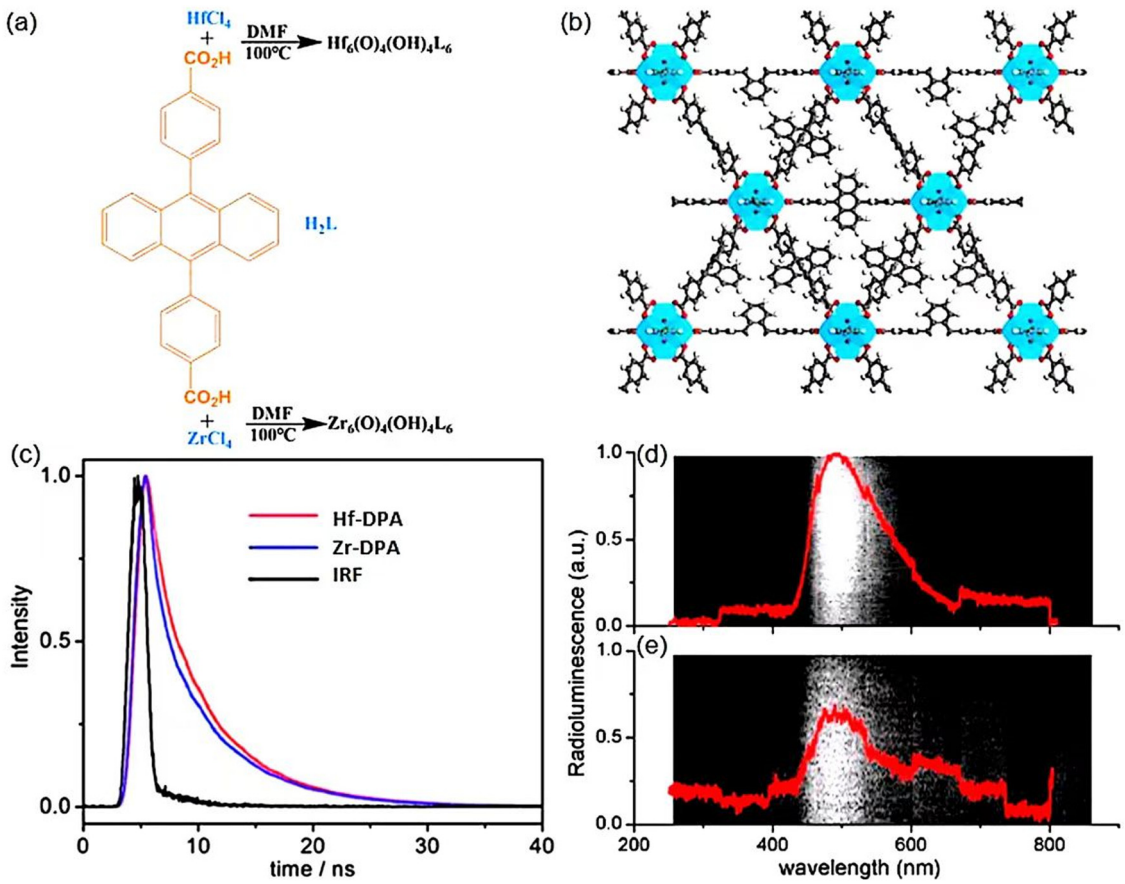

Fig. 9 (a) Preparation methods for **Hf-DPA** and **Zr-DPA**. (b) Structural representations along the [110] directions. (c) Fluorescence decay profiles over time for **Hf-DPA** (red), **Zr-DPA** (blue), and DPA ligand (black) suspensions in water excited at 368.8 nm and monitored at 469 nm, with instrument response function (IRF, gray). Optical spectra of (d) **Hf-DPA** and (e) **Zr-DPA** following exposure to X-rays at a dose rate of 6 Gy min^{-1}, captured using an EM-CCD camera with Light field software. Reprinted with permission.[62] Copyright 2014, American Chemical Society.

light emitting diodes (LEDs) and lasers, perovskite can provide high color purity of light, which is very important for display technology and lighting fields.[63] Perovskite materials are also known for their high photoelectrical conversion efficiency, which also makes them potentially useful in X-ray detector components.[50,63] For instance, Zheng *et al.* demonstrated that $CsPbBr_3$ perovskite nanocrystals (PNCs) stabilized with poly-(maleic anhydride-*alt*-1-octadecene) (PMAO) exhibit a characteristic

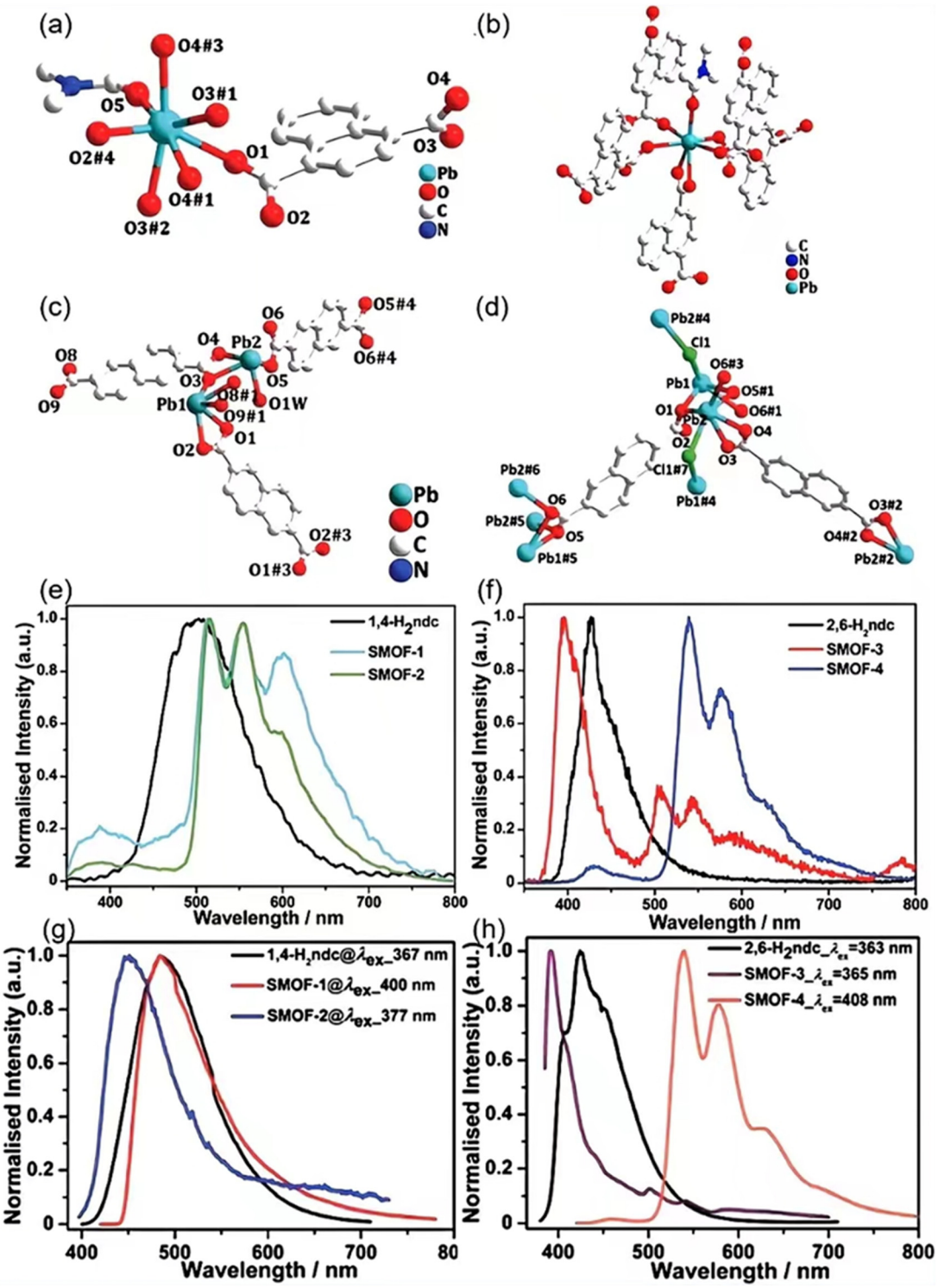

Fig. 10 Pb(II) coordination within **Pb-SMOF-1** (a), **Pb-SMOF-2** (b), **Pb-SMOF-3** (c), **Pb-SMOF-4** (d). The XSL spectra of 1,4-H_2ndc, **Pb-SMOF-1** and **Pb-SMOF-2** (e) and 2,6-H_2ndc, SMOF-3 and SMOF-4 (f). The peak steady-state PL spectra of free 1,4-H_2ndc and **Pb-SMOFs 1–2** (g), and 2,6-H_2ndc and **Pb-SMOFs 3–4** (h). Reprinted with permission.[64] Copyright 2019, Royal Society of Chemistry.

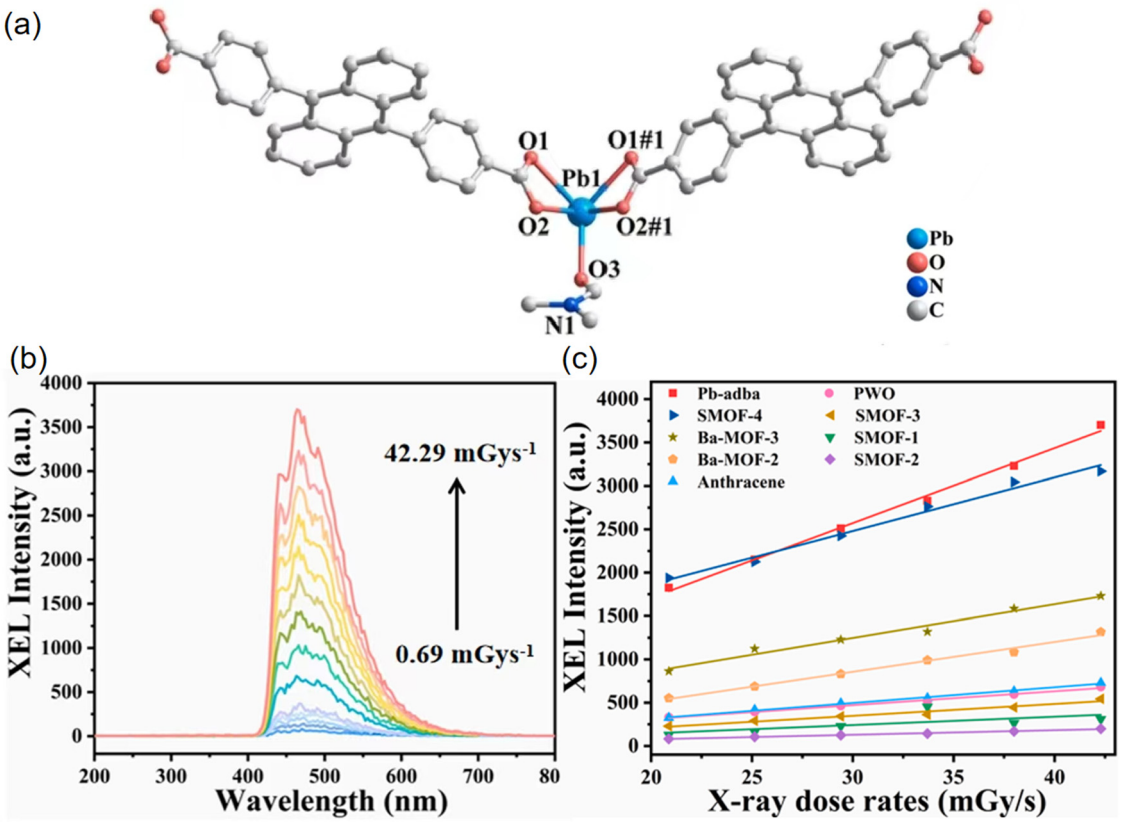

Fig. 11 (a) Coordination environments of the Pb^{2+} ion. (b) The XEL spectra in the dose rate range of 0.69–42.29 mGy s^{-1} at a voltage of 50 kV. (c) Linear correlation between XEL intensity and dose rate for **Pb-adba**, PWO, anthracene crystals, and other documented scintillating MOFs. Reprinted with permission.[60] Copyright 2022 Elsevier.

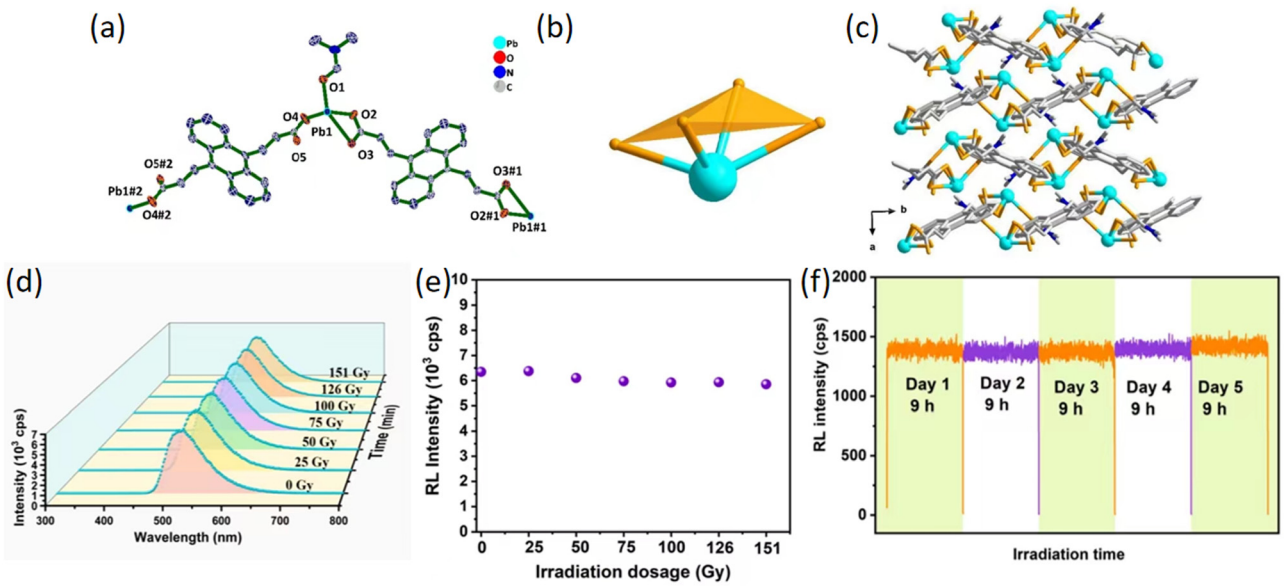

Fig. 12 (a) The coordination environment of Pb^{2+} centers in **Pb-adda**. The symmetry operations are defined as #1 1 − *x*, 2 − *y*, 2 - *z*; #2 1 − *x*, 2 − *y*, 1 − *z*. (b) The hemi-directed geometrical configuration of Pb in **Pb-adda**. (c) Viewing the **Pb-adda** structure along the *c*-axis reveals its arrangement, with Pb ions colored turquoise, oxygen in light orange, carbon in light gray, and nitrogen in blue. Hydrogen atoms are not shown for better visibility. (d) The RL spectra of **Pb-adda** after different X-ray dose irradiation. (e) A graph depicting the relationship between the X-ray-induced signal intensity of **Pb-adda** and the dosage of irradiation. (f) The stability chart illustrating the performance of **Pb-adda** after continuous exposure to X-rays at a rate of 12.40 mGy s^{-1} for five consecutive days, totaling nine hours of daily exposure. Reprinted with permission.[61] Copyright 2021, Elsevier. Similar articles are ref. 66.

blue emission peak at approximately 430 nm under X-ray excitation. This emission peak indicates that the PMAO-PNCs can effectively convert X-ray energy into visible light. Furthermore, fluorescent flexible films prepared by mixing PMAO-PNCs with PDMS-NH_2 are capable of clearly displaying the internal line structure of an electronic chip under X-ray irradiation, achieving a resolution as high as 5 lp mm^{-1}, which demonstrates their excellent X-ray imaging performance.[63]

The Pb-MOF design leverages the high atomic number and X-ray attenuation coefficient of lead(II) ions to create efficient X-ray absorption hubs. It also integrates organic ligands featuring extensive π-electron systems to boost luminescent efficiency. These materials are poised for use in X-ray detection and imaging, particularly in applications that necessitate high sensitivity and rapid response. By fine-tuning the composition and structure of Pb-MOF, the X-ray scintillation performance can be optimized.

For example, in 2019, Lu *et al.* used Pb^{2+} ions for X-ray absorber and naphthalene dicarboxylate (ndc^{2-}) as the photoluminescent centers in the fabrication of crystalline SMOFs ($[Pb(1,4\text{-ndc})(DMF)]_n$ (**Pb-SMOF-1**), $[Pb(1,4\text{-ndc})(DMA)]_n$ (**Pb-SMOF-2**), $[Pb_2(2,6\text{-ndc})_2(H_2O)]_n{\cdot}n$DMF (**Pb-SMOF-3**) and $[Pb_4(2,6\text{-ndc})_3Cl_2]_n$ (**Pb-SMOF-4**), where 1,4-ndc^{2-} = 1,4-naphthalene dicarboxylate, 2,6-ndc^{2-} = 2,6-naphthalene dicarboxylate) (Fig. 10a–d).[64] Fig. 10e and f shows that Pb(II) based MOFs have good luminescent properties in X-ray detection, especially **Pb-SMOF-4**, which shows excellent X-ray conversion ability and luminescent efficiency due to its solvent-free and denser structure. The X-ray stimulated luminescence (XSL) findings underscore the complementary actions between the heavy metal Pb(II) ions, acting as efficient X-ray absorbents, and the organic ligands, acting as light-emitting units. This integration confers on these Pb(II)-MOFs advantageous characteristics as scintillators for the detection of X-rays. Furthermore, the maximum emission peaks observed for **Pb-SMOF-1** and **Pb-SMOF-2** are primarily attributed to charge transfer occurring at the center of the ligand, as indicated by their half-height full width being consistent with that of the free ligand. By altering the excitation wavelength, additional emission peaks emerge in the emission spectra of **Pb-SMOF-1** and **Pb-SMOF-2** (Fig. 10g and h). The solid-state emissions observed under various excitation wavelengths, supplemented by density of state analyses and density functional theory (DFT) calculations, illuminate the scintillating spectral characteristics. These findings suggest that the scintillation triggered by X-rays is dependent on the electronic configurations of the luminescent materials and the surroundings in which they are located.

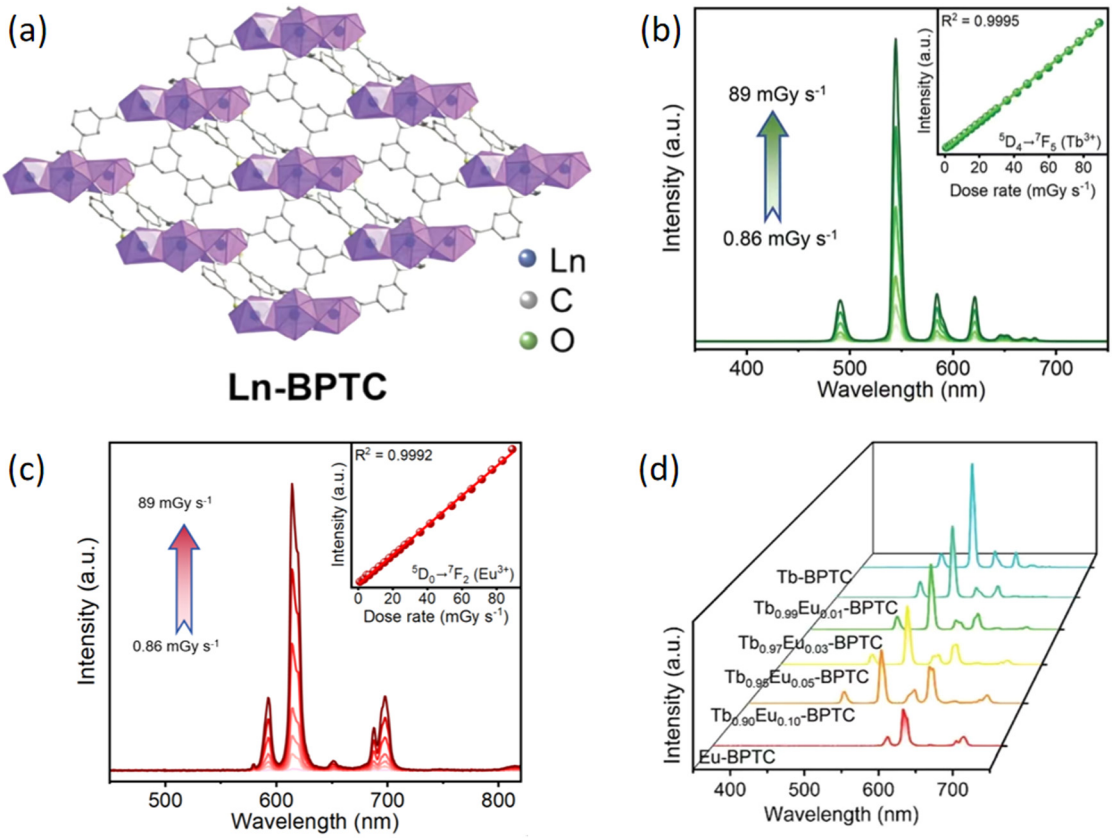

Fig. 13 (a) The crystal structure of **Ln-BPTC**. (b) The XEL spectra for **Tb-BPTC** at several X-ray dose rates, spanning from 0.86 to 89 mGy s^{-1} at ambient temperature, with the insets highlighting the strong linear correlation between XEL intensity and X-ray dose rate. (c) The XEL spectra of **Eu-BPTC** at various X-ray dose rates, extending from 0.86 to 89 mGy s^{-1} at room temperature, with the insets illustrating the robust linear correlation between XEL intensity and X-ray dose rate. (d) The XEL spectra of the as-prepared **Ln-BPTC MOFs** with differing molar ratio of Tb^{3+} and Eu^{3+}. Reprinted with permission.[67] Copyright 2024, Wiley.

On the other hand, in 2022, Xie *et al.* constructed a Pb^{2+} MOF $[Pb(adba)(DMF)]_n$ (**Pb-adba**) using H_2adba (H_2adba = 4,4′-(9,10-anthracenediyl) dibenzoic acid).[60] Lead is known for its significant X-ray absorption cross section, which is crucial for achieving high X-ray absorption efficiency.[65] In **Pb-adba**, the Pb^{2+} ion coordinated to five oxygen atoms from four carboxylate groups of two ligands and one DMF molecule (Fig. 11a). The XEL intensity of **Pb-adba** progressively rises with varying radiation dose rates ranging from 0.69 to 42.29 mGy s^{-1}, indicating a robust response to X-rays (Fig. 11b). As shown in Fig. 11c, **Pb-adba** exhibits a notably higher X-ray response sensitivity (k = 86.35) compared to PWO ($PbWO_4$) (k = 16.03), anthracene (k = 18.13), and various reported SMOFs. This superior performance is attributed to the synergistic effect of the heavy metal Pb, which has effective X-ray absorption, and the anthracene-derived organic ligand, which offers efficient luminescence. **Pb-adba** displays a favorable linear response, detection sensitivity, and commendable resistance to X-ray irradiation.

More recently, in 2022, Wang *et al.* constructed the SMOF $[Pb(adda)(DMF)]_n$ (**Pb-adda**) (H_2adda = (2E,2′E)-3,3′-(anthracene-9,10-diyl) diacrylic acid, DMF = *N*,*N*-dimethylformamide) with X-ray response by a simple solvothermal synthesis.[61] This material emits an intense green light under ultraviolet or X-ray exposure, discernible to the unaided eye. Each Pb(II) ion in Pb-MOF is surrounded by four oxygen atoms, with two from carboxylate groups and one from a DMF molecule, resulting in Pb–O bond distances ranging from 2.329(2)–2.723(2) Å (Fig. 12a–c). All ligands in **Pb-adda** adopt a *trans* conformation, presenting central symmetry. The RL spectra of **Pb-adda** were gathered following various X-ray dosages. As depicted in Fig. 12d and e, there was no significant change in peak position or shape after a 151 Gy irradiation, with the RL intensity retaining approximately 96% of its original value. Furthermore, after continuous exposure to an X-ray dose rate of 12.40 mGy s^{-1} for 9 hours daily over a period of five days, there was no noticeable decrease in light intensity or quenching (Fig. 12f). This characteristic is also evident when comparing the stability of **Pb-adda** with other reported lead-based MOF scintillators (**Pb-SMOF-1** and **Pb-SMOF-2**) and conventional scintillators (BGO, $(Lu,Y)_2SiO_5:Ce^{3+}$ and organic crystal anthracene). Concurrently, leveraging the good chemical compatibility of Pb-MOF with dispersing agents, the incorporation of Pb-MOF into a polymer matrix yields a pliable composite film suitable for X-ray imaging applications.

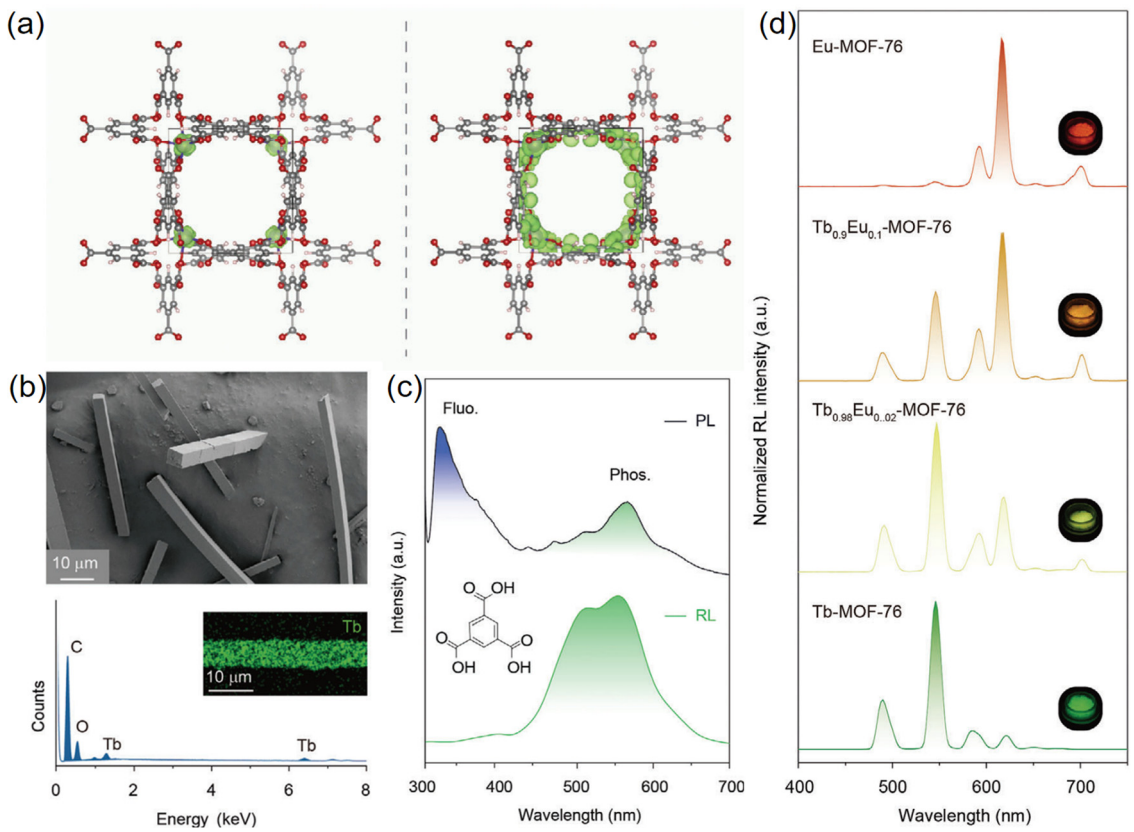

Fig. 14 (a) Calculated partial charge densities (in green) of the VBM (left) and CBM (right) of **Tb-MOF-76** microcrystals. X-ray-excited RL in lanthanide metal–organic frameworks. (b) A composite image of **Tb-MOF-76** microcrystals featuring a scanning electron microscopy image (at the top) and energy-dispersive X-ray spectroscopy analysis (at the bottom). The inset shows the even distribution of the Tb element within a specific **Tb-MOF-76** microcrystal. (c) Displaying the normalized PL and RL spectra of H_3BTC molecules, with purple and green bands indicating the fluorescence and phosphorescence of H_3BTC molecules, respectively. (d) RL responses of MOF-76 micro-crystals doped with varying concentrations of Tb^{3+} and Eu^{3+} dopants, along with images of MOF-76 microcrystals under X-ray exposure. Reprinted with permission from ref. 68. Copyright 2023, Wiley.

3.3.3. Ln-MOF. The lanthanides have unpaired 4f electrons that can produce a variety of luminescent colors, suitable for multi-color imaging and sensing. Although lead-based MOFs have a very broad range of applications in the X-ray field, attributed to their robust X-ray absorption capacities, lanthanide MOFs likewise possess their distinctive advantages. These include the exceptional optical properties of lanthanides, characterized by sharp emission lines and substantial Stokes shifts. In certain instances, lanthanide MOFs may offer superior biocompatibility and reduced toxicity, coupled with a diverse array of elements and luminescent properties that add to their allure.

For instance, in 2024, Li *et al.* proposed a new strategy of introducing the radio-luminescent functional building units (RBUs) concept to develop self-calibrating radio-luminescent thermometer based on Ln-MOFs scintillator. As demonstrated in Fig. 13a, RBUs including Tb^{3+}, Eu^{3+}, and the organic ligand [1,1′-biphenyl]-3,3′,5,5′-tetracarboxylic acid (H_4BPTC) were selected to construct a series of isomorphic MOFs, named **Ln-BPTC**.[67] Due to the good coordination abilities and reasonable energy levels design of RBUs, **Ln-BPTC** exhibited excellent photo- and radio-luminescent properties. Due to the introduction of high-Z metal nodes (Tb^{3+}/Eu^{3+}) into the framework, the radio-luminescent properties of the **Ln-BPTC** were investigated under the X-ray irradiation. Fig. 13b and c displays the XEL spectra of **Tb-BPTC** and **Eu-BPTC**, respectively, under a relative wide range of X-ray dose rate from 0.86 to 89 mGy_{air} s^{-1} at room temperature. Excellent linearity between XEL intensity and X-ray dose rate can be obtained, which means that the scintillation response and the radiation intensity can be predictably correlated, benefiting the good X-ray image contrast. By adjusting the ratio of Eu^{3+}/Tb^{3+} ions, the emission spectra can be modulated, resulting in a transition of the emitted light color from green to red, as depicted in Fig. 13d. This allows for self-calibrating detection based on ratiometric XEL intensities, offering high sensitivity in both absolute and relative terms. Furthermore, the researchers explored the X-ray imaging application using the as-synthesized MOF-based membranes, which exhibited excellent spatial resolution, with a maximum of approximately 18-line pairs per millimeter. Notably, the $Tb_{0.95}Eu_{0.05}$-BPTC membrane showcased its potential in *in situ* thermoresponsive X-ray imaging.

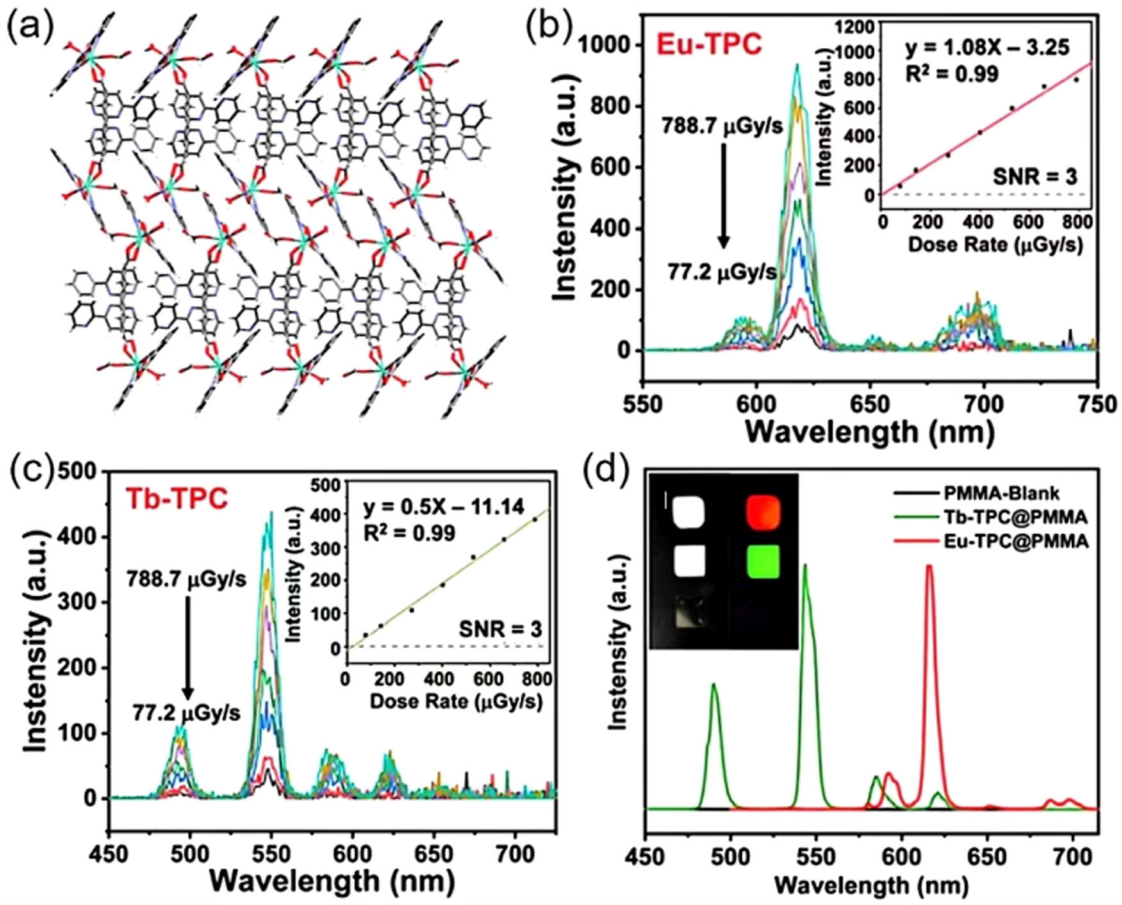

Fig. 15 (a) Two-dimensional layered structure. The XEL spectra of **Eu-TPC** and **Tb-TPC** in their crystalline form at room temperature, with insets showing the linear relationship between XEL intensity and X-ray dose rate at wavelengths of (b) 619 nm and (c) 543 nm. (d) Normalized XEL spectra of the **Eu-TPC** film, **Tb-TPC** film and PMMA film at room temperature, with insets presenting photographs of the films at bright field (left column) and under X-ray irradiation (right column). Reprinted with permission.[9] Copyright 2023, Royal Society of Chemistry.

In another notable study, Zhang *et al.* constructed the lanthanide-based MOFs (**Ln-MOF-76**; Ln = Tb or Eu) using 1,3,5-benzenetricarboxylate (H_3BTC) (Fig. 14b).[68] In the particular instance of **Tb-MOF-76**, the maximum of the valence band is predominantly made up of Tb 4f orbitals, indicating a likely occurrence of hole capture (Fig. 14a). The mechanistic insights from the study propose that lanthanide ions, upon X-ray absorption, create a high-density of molecular triplet excitons. These excited linkers then sensitize the lanthanide ions through a nonradiative resonance energy transfer process.

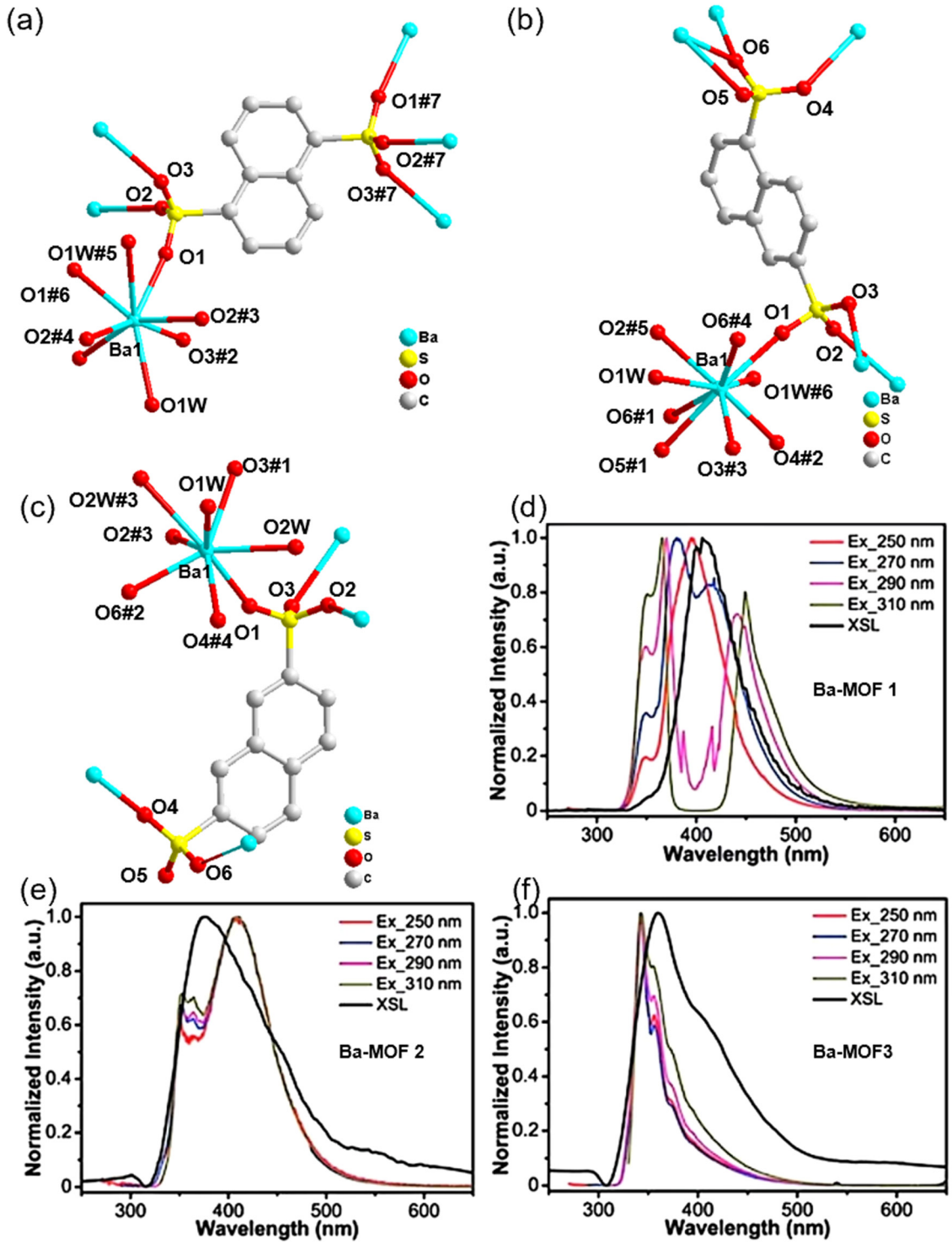

Fig. 16 The coordination environments within (a) **Ba-MOF 1**, (b) **Ba-MOF 2** and (c) **Ba-MOF 3**. The solid-state PL spectra and X-ray stimulated luminescence spectra of (d) compound **Ba-MOF 1**, (e) compound **Ba-MOF 2**, (f) compound **Ba-MOF 3**. Reprinted with permission.[70] Copyright 2021, Royal Society of Chemistry.

The design of Ln-MOFs strategically leverages the high-density triplet excitons to sensitize lanthanide emitters, leading to the production of intense RL. Fig. 14c illustrates the generation of triplet excitons under X-ray excitation, measured by comparing the PL and RL spectra of H_3BTC molecules. Furthermore, Fig. 14d showcases the RL of MOF-76 microcrystals at varying doping concentrations of Tb^{3+} and Eu^{3+}. The study also explored the capability of achieving emission color regulation through the co-doping approach. The crystallographic structure provides a delocalized electronic property instead of discrete subunits, facilitating the direct capture of charge carriers by lanthanide-based luminophores. Zhao *et al.* also reported similar works that utilized a lanthanide MOF to achieve efficient scintillation.[69]

In another interesting example, Liu *et al.* synthesized a pair of innovative one-dimensional linear metal–organic CPs (**Eu-TPC** and **Tb-TPC**) (Fig. 15a) using the organic ligand (2,2′:6′,2″-terpyridine-4′-carboxylic acid, TPC).[9] These high-Z lanthanide atoms within the CPs are capable of efficiently converting high-energy X-rays into their characteristic visible light emissions. This transformation is facilitated by the energy bridge effect of the organic ligands, which enhances the overall light emission by improving the conversion efficiency. The luminescent spectra of **Eu-TPC** and **Tb-TPC** under X-ray stimulation demonstrated the distinctive peaks of Eu^{3+} and Tb^{3+} ions, respectively, akin to their emission spectra when excited by 365 nm light (Fig. 15b and c). As the X-ray dose rate augments, there is a proportional escalation in luminescent intensity. The XEL spectra of these films also revealed the signature peaks of Eu^{3+} and Tb^{3+} cations (Fig. 15d). Notably, the red and green luminescence emitted by these CPs was discernible to the naked eye under X-ray irradiation at room temperature. They blended **Eu-TPC** and **Tb-TPC** microcrystals with polymethyl methacrylate (PMMA) polymers to prepare flexible scintillation films by drop-coating and demonstrated the concept of their application in high-resolution X-ray imaging.

3.3.4. Ba-MOF. Although barium-based MOFs are less common than lead-based MOFs in X-ray applications, they also have their own unique applications in specific fields. Ba-MOF achieves efficient X-ray detection and energy resolution through carefully designed organic ligands and metal node, demonstrating potential applications in the field of scintillation materials.

In 2021, Lu *et al.* constructed the compounds $[Ba(1,5\text{-nds})H_2O]_n$ (**Ba-MOF 1**), $[Ba(1,6\text{-nds})H_2O]_n$ (**Ba-MOF 2**) and $[Ba(2,7\text{-nds})(H_2O)_2]_n$ (**Ba-MOF 3**) using luminescent *p*-conjugated naphthalene disulfonates (nds^{2-}).[70] The coordination environments of the Ba^{2+} ions and nds^{2-} linkers are presented in Fig. 16a, b, c. As illustrated in Fig. 16d–f, compounds **Ba-MOFs** all showed their characteristic luminescence. The X-ray

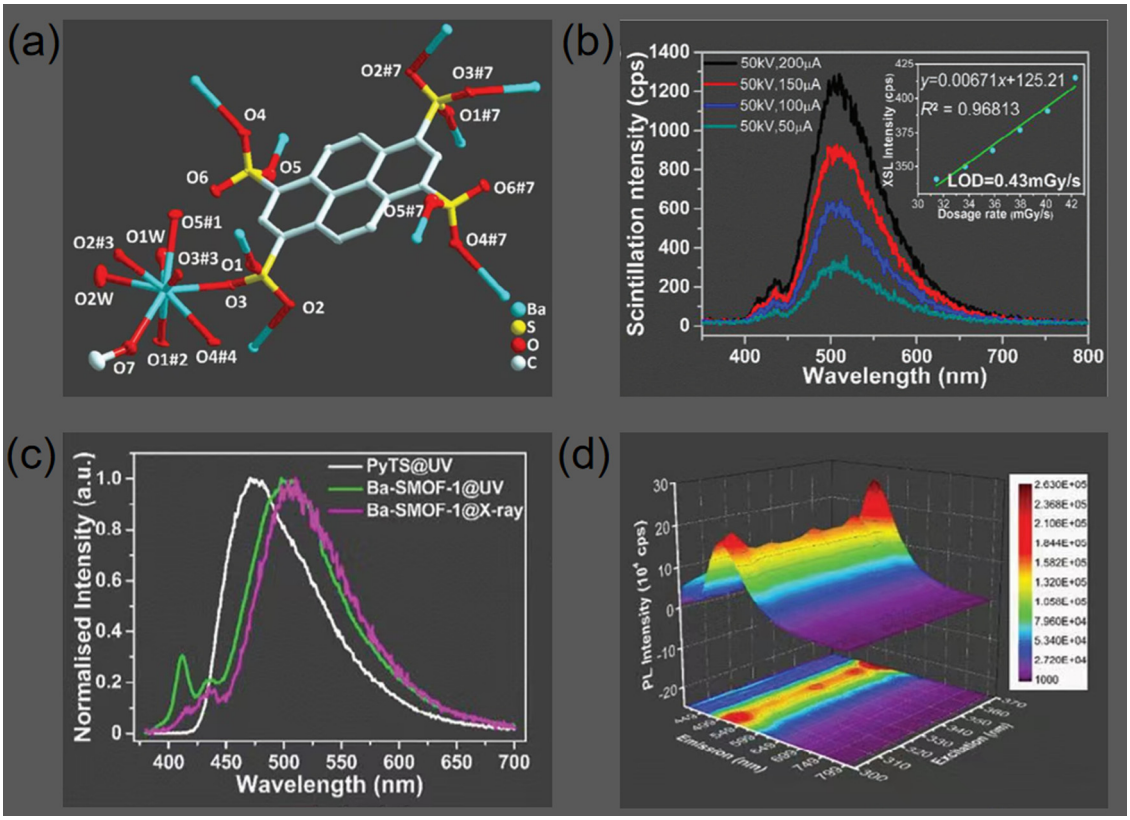

Fig. 17 (a) The coordination environments of $PyTS^{4-}$ ligand and Ba^{2+} ions in **Ba-SMOF**. (b) XSL spectra with X-ray dosage rate detection performance inset. (c) Solid-state photoluminescent spectra for free ligands Na_4PyTS and **Ba-SMOF**, along with XSL spectra for **Ba-SMOF**. (d) Solid-state synchronization fluorescence spectra for **Ba-SMOF** with gradient scanning step of 5 nm. Reprinted with permission.[71] Copyright 2024, Wiley.

excitation luminescence spectrum of compound **Ba-MOF 1** shows a wide and intense emission band of about 408nm, while its PL spectrum shows multimodal behavior varying with excitation wavelength. The XEL spectra of compounds **Ba-MOF 2** and **Ba-MOF 3** show weak emission at 358 nm and 380 nm, respectively, and their PL spectra also show fixed narrow emission peaks. The 1,5-H_2nds ligand shows similar emission characteristics to compound **Ba-MOF 1** under solid state and X-ray excitation, indicating that the ligand plays a key role in the luminescence process. In the pulsed height X-ray excited luminescence spectra, the three **Ba-MOFs** exhibit consistent energy resolution, suggesting that these materials possess a potential homogeneity advantage for detecting high-energy ionized particles.

More recently, Lu *et al.* utilized a pyrene-derived organic ligand and Ba(II) salts to synthesize the compact X-ray scintillating **Ba-SMOF 1** ($[Ba_2(PyTS)(CH_3OH)_2(H_2O)_4]_n$),[71] where $PyTS^{4-}$ denotes pyrene-1,3,6,8-tetrasulfonate. Ba, recognized for its elevated atomic number (Z), serves as a suitable alternative for the effective absorption of ionizing X-rays, avoiding the hazards associated with toxicity of lead and the radioactivity of uranyl ions.[70] As depicted in Fig. 17a, the sulfonate groups of the $PyTS^{4-}$ ligands in **Ba-SMOF 1** exhibit two distinct coordination modes. The continuous electron density within the $PyTS^{4-}$ dimers is characterized as associative exciton behavior, which is enhanced by the coordinated methanol molecules. This unique feature results in the coexistence of both static and dynamic excimer emissions in **Ba-SMOF 1**. The XSL spectra of **Ba-SMOF 1** exhibited a predominant emission peak centered at approximately 505 nm, accompanied by subsidiary peaks in the blue region of the emission spectrum (Fig. 17b). Fig. 17c illustrates the remarkable similarity between the PL and XSL spectra of **Ba-SMOF 1**. Solid-state synchronization fluorescence spectroscopy corroborates the coexistence of dynamic and static emissions of $PyTS^{4-}$ ligand in **Ba-SMOF 1** (Fig. 17d). The main emission peak, associated with dynamic emission, is invariant with varying excitation wavelengths, while the minor peaks, associated with static emissions, are also consistent. The X-ray ionizing radiation appears to induce a minor bathochromic shift in the principal emission band owing to the generation of excited electron–hole pairs, or excitons.[72]

To provide a clear overview of MOF-based scintillator materials, we have summarized the reported materials along with their composition, luminescent wavelength, light yield, fluorescence decay time, detection limit, and imaging resolution in Table 1.

Table 1 A summary of reported MOF-based scintillator materials

Entry	Metal ion	Ligand	Luminescent wavelength (nm)	Light yield (photons MeV^{-1})	Fluorescence decay time (μs)	Detection limit (μGy s^{-1})	Imaging resolution (lp mm^{-1})	Ref.
1	Cu^+	4,6-dimethylpyrimidine-2-thione	735	3721	13.7	<5.5	—	49
2	Cu^+	OBP	560	41 000	—	34.6	20	51
3	Cu^+	2-(alkylsulfonyl)pyridines	562	—	0.4–2.0	—	—	52
4	Cu^+	I^-	452	—	—	0.063	7.3	50
6	Ca^{2+}	H_2L^1 H_2L^2	478 442	—	0.0082 0.00148	—	—	53
7	Zr^{4+}	DPA	440	821	0.0033	—	—	56
8	Zr^{4+}	TADF chromophore	—	—	—	0.256	—	57
9	Zr^{4+}	H_4ETTC	535	—	0.0037	1.6	>14.3	58
10	Sr^{2+}	H_2DOBPDC	430	3323	0.00186	4.96	5	59
11	Hf^{4+} Zr^{4+}	DPA	400–600	—	0.00619 0.00596	—	—	62
12	Pb^{2+}	PMAO	520	—	0.00677	—	—	63
13	Pb^{2+}	1,4-H_2ndc	494(DMF) 451(DMA)	—	0.00161 0.01345	—	—	64
14	Pb^{2+}	2,6-H_2ndc	390(DMF) 536(DMA)		0.00398 32.95			64
15	Pb^{2+}	H_2adba	470	—	0.00557	390	—	60
16	Pb^{2+}	H_2adda	512	—	0.0029	—	5.5	61
17	Tb^{3+} Eu^{3+}	H_4BPTC	544	38800	0.00241	0.1561	16.5	67
18	Tb^{3+} Hf^{4+}	*Meso*-tetra(4-carboxyphenyl) porphine	702	—	550	—	—	73
19	Tb^{3+} Eu^{3+}	H_3BTC	—	—	—	0.023	16.6	68
20	Tb^{3+}	HNIC	547	29 379	1520	0.452	12.6	69
21	Eu^{3+} Tb^{3+}	TPC	—	6121 5453	463 000 134 000	5200 11 140	5.15 4.46	9
22	Tb^{3+}	4,4′,4″-*s*-triazine-1,3,5-triyltri-*p*-aminobenzoate	623	—	256.5	4.42	—	74
23	Ba^{2+}	5-nds^{2-}, 1,6-nds^{2-}, 2,7-nds^{2-}	408, 380, 358	—	—	—	14.95% 28.42% 24.72%	70
24	Ba^{2+}	$PyTS^{4-}$	505	—	0.00117	430	—	71

All of these representative studies are discussed in detail within this review.

4. Applications of MOF-based X-ray scintillators

The typical applications of MOF-based X-ray scintillators in a wide range of fields such as high sensitivity and high-resolution X-ray detector, flexible imaging and X-ray radiation therapy are discussed.

4.1. High sensitivity and high-resolution X-ray detector

High-sensitivity detectors can obtain clear images at lower X-ray doses, reducing radiation harm to patients or objects being detected, and advancing the development of medical imaging and safety detection technologies. Similarly, high-resolution detectors are becoming increasingly crucial as the demand for fine machining and micro- and nanofabrication grows. For instance, Zhang *et al.* measured the radiation intensity of Tb-MOFs scintillators and observed a linear correlation with the X-ray irradiation dose rate over a wide range (Fig. 18a). The calculated detection limit was 23 nGy s^{-1}. Additionally, Tb-MOF-76 scintillators can efficiently convert X-rays into tunable visible light.[68] These micro-scintillators are characterized by outstanding photostability, elevated photoconversion efficiency, and significant spectral modulation capabilities, which facilitate the creation of pliable scintillators that deliver superior visualization and imaging capabilities. The flexible X-ray detector based on Tb-MOF-76 achieves a high spatial resolution exceeding 16.6 lp mm^{-1} and a modulation transfer function (MTF) of 0.2, markedly surpassing the performance of traditional flat-panel X-ray detectors (Fig. 18b). This enhanced performance is likely due to the even distribution of Tb-MOF-76 microcrystals, which minimizes light scattering. The effectiveness of X-ray imaging was further illustrated through the imaging of a ceramic fuse and a fish (Fig. 18c and d).

More recently, Wang *et al.* proposed that In^{+} doping improves the efficiency of carrier capture, and yields high light output, high sensitivity X-ray detection crystal materials. Objects such as a spring within capsule and miniature electronic parts were imaged using both pristine and 0.2% indium-doped $Cs_3Cu_2I_5$ SCs-based X-ray imaging system, resulting in high-definition X-ray photographs depicted in Fig. 19a and b. The undoped $Cs_3Cu_2I_5$ scintillator-based imaging system exhibits a high spatial resolution of 16 lp mm^{-1}, while the 0.2% In-doped sample demonstrates an even higher spatial resolution of 18 lp mm^{-1}.[54] They measured the RL of a 125 μm thick scintillation screen at various X-ray dose rates (Fig. 19c). The

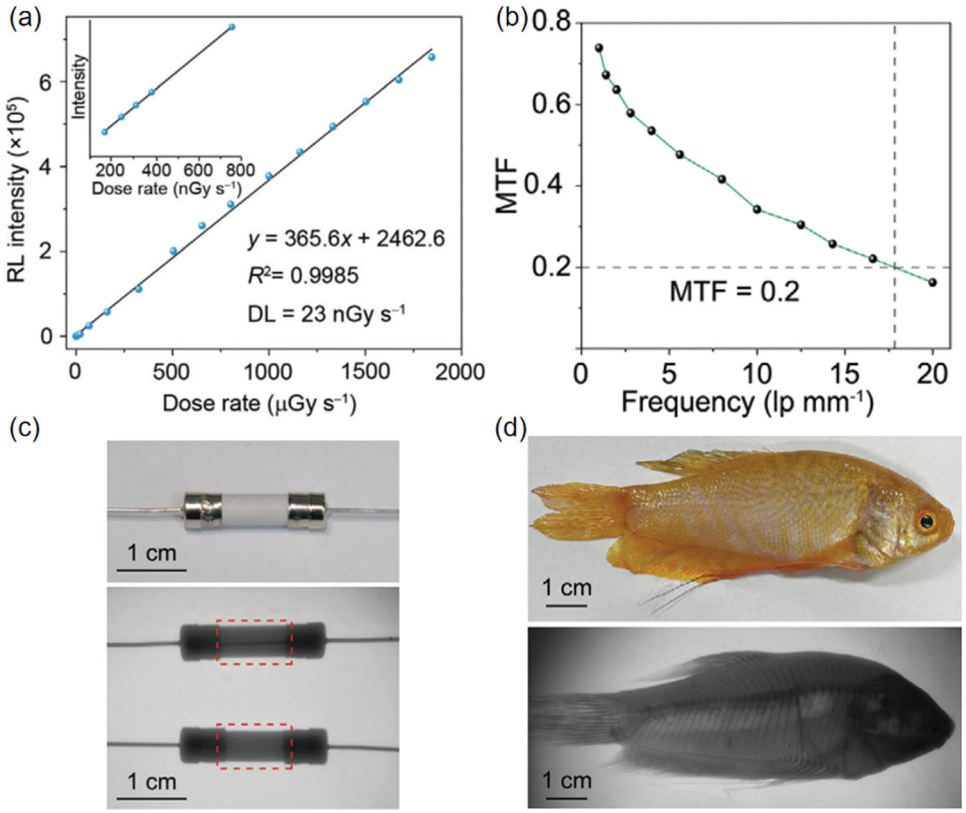

Fig. 18 (a) The radioluminescence intensity of Tb-MOF-76 microcrystals was recorded as a function of the dose rate. The detection limit was calculated to be 23 nGy s^{-1}, with a signal-to-noise ratio of 2.85. An enlarged view of the data in the range of 100–800 nGy s^{-1} is provided as an inset. (b) MTF values of the Tb-MOF-76 film, as determined by the line pair pattern method. (c) Bright-field image of a ceramic fuse (top) and comparative X-ray images of its inner structure before and after blowing (bottom). (d) Photographs of a fish in both bright-field (top) and dark-field (bottom) conditions, before and after exposure to X-rays. Reprinted with permission.[68] Copyright 2023, Wiley.

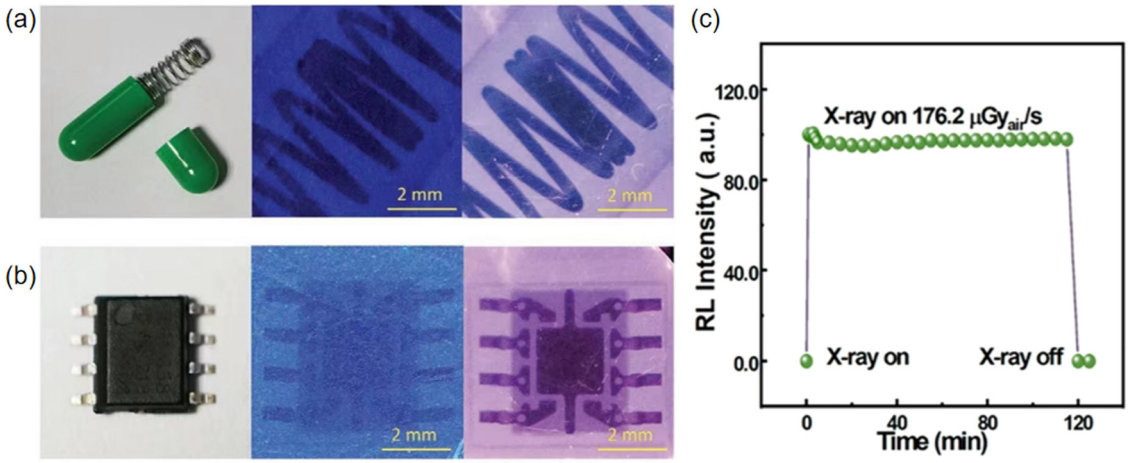

Fig. 19 X-ray imaging of $Cs_3Cu_2I_5$: In. (a) a spring in a capsule shell and (b) a small electronic component using undoped $Cs_3Cu_2I_5$ (in the middle) and In^+-doped $Cs_3Cu_2I_5$ (on the right) SCs. (c) The RL intensity of the $Cs_3Cu_2I_5$–PSS screen is directly proportional to the X-ray dose rate. Reprinted with permission.[54] Copyright 2022, Wiley.

results showed a strong linear correlation, which is beneficial for achieving high X-ray image contrast. The minimum detection limit was determined to be 63 nGy_{air} s^{-1}, derived from the slope of the radioluminescence fitting curve at low dose rates with a signal-to-noise ratio of 3. This is 87 times lower than the typical X-ray diagnostic dose of 5.5 μGy_{air} s^{-1}.

4.2. Flexible imaging

Flexible X-ray imaging is an advanced imaging technique that uses flexible X-ray detectors or luminaires to capture X-ray images. It is able to provide high-resolution images, which is crucial for detecting tiny defects or details. It can also be used in extreme environments, such as high humidity or large temperature changes, without compromising imaging performance. The regular arrangement and uniformity of MOF scintillators contribute to high resolution imaging. Flexible imaging devices, constructed on a PDMS substrate, can be integrated not only with rare earth elements but also with copper (Cu) metals to form highly efficient scintillators. For instance, Zhang *et al.* selected various inorganic specimens to assess the practical imaging

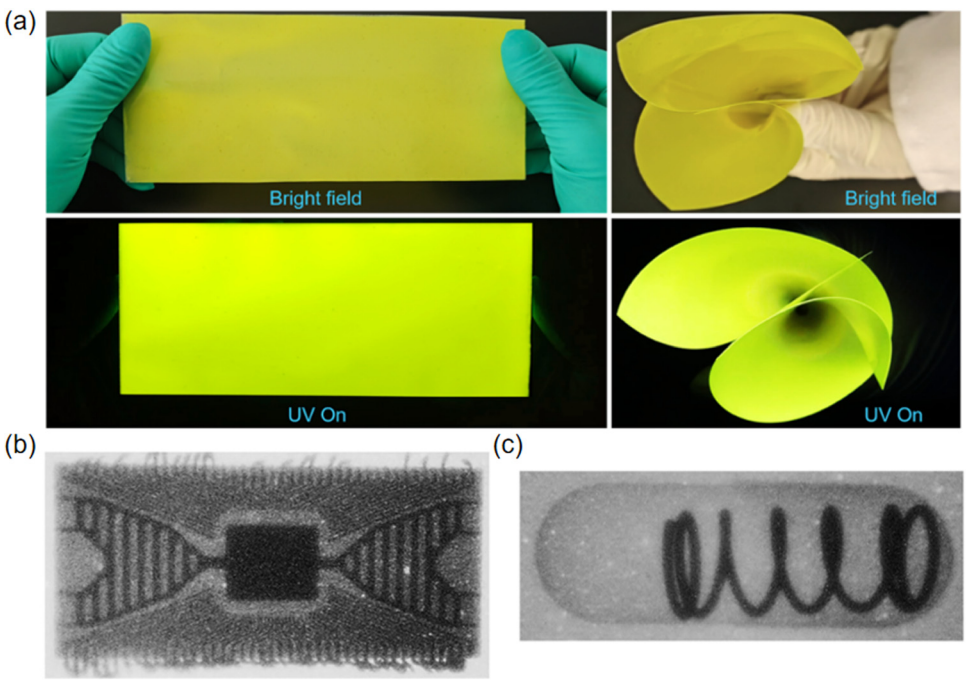

Fig. 20 (a) Photographs of the composite YPCN-94@PDMS membrane under sunlight and UV light and demonstration of flexibility. (b) X-ray imaging of a chipboard by utilizing the Y-PCN-94@PDMS composite scintillating membrane; and (c) X-ray imaging of a spring-loaded pill with the application of the Y-PCN-94@PDMS composite scintillating membrane. Reprinted with permission.[58] Copyright 2023, American Chemical Society.

Fig. 21 (a)–(c) Visual representations of imaging for a ballpoint pen, sunflower kernel, and microchip; (d) Depicting a mock security inspection process with the scintillator screen; (e) Dynamic flexible X-ray imaging system and real-time imaging photographs of circuit boards. Reprinted with permission from ref. 51. Copyright 2023, Wiley.

capabilities of the Y-PCN-94@PDMS composite membrane.[58] As shown in Fig. 20a, the composite Y-PCN-94@PDMS membrane presents superior flexibility stemming from PDMS. As shown in Fig. 20b and c, the intricate details of both a circuit board and a pressure-sensitive tablet were distinctly rendered by the composite Y-PCN-94@PDMS membrane. Utilizing the blade-coating method, the pliable YPCN-94@PDMS scintillating membrane was efficiently produced and employed for X-ray imaging, achieving an imaging resolution exceeding 14.3 lp mm^{-1}.

In another study, Peng *et al.* combined **Cu-MOF 1-rod** with PDMS to construct a pliable scintillation screen that achieved dynamic X-ray imaging of actual objects at a imaging resolution of 20 lp mm^{-1}, significantly surpassing the resolution of previously reported flexible scintillating screens that possess tensile strength.[51] This scintillation screen was utilized for X-ray imaging of various items, including a ballpoint pen with an internal spring, a sunflower kernel with lighter components, and a microchip with intricate circuitry (Fig. 21a–c). Upon X-ray stimulation, the internal structures of these items were distinctly captured on the scintillation screen. Additionally, a suitcase containing metal objects was used for a security testing scenario. As shown in Fig. 21d, the metal wrench, key, and screw within the suitcase were clearly discernible on the scintillation screen under X-ray exposure. Furthermore, Fig. 21e presents the ability of the flexible imaging device to operate at multiple angles (0°, 90°, 180°), demonstrating that the device is capable of dynamic imaging by capturing X-ray images of moving objects. The illustration on the right depicts how X-rays penetrate the MOF crystal and are subsequently detected, which is a key step in enabling the imaging process.

4.3. X-ray radiation therapy

X-ray radiation therapy is a widely used method for cancer treatment that inhibits growth and reproduction by using X-rays, gamma rays or particle beams to damage the DNA of tumor cells.[72] Nanoscale MOF (nMOF) based on heavy metals are excellent radiosensitizers in radiotherapy by increasing energy deposition and reactive oxygen species (ROS) production. Therefore, heavy metal nMOF containing covalently bound drugs can be effectively triggered by X-rays. Xu *et al.* constructed a novel nano-metal–organic framework material, Hf-TP-SN.[75] Its organic ligand is covalently bound to 7-ethyl-10-hydroxycamptocampine (SN38) and can be triggered by X-rays to release SN38, so Hf-TP-SN can be used in radio-chemical synergistic therapy. Under X-ray irradiation, electron dense Hf_{12}SBU in Hf-TP-SN can be used as a radiosensitizer to

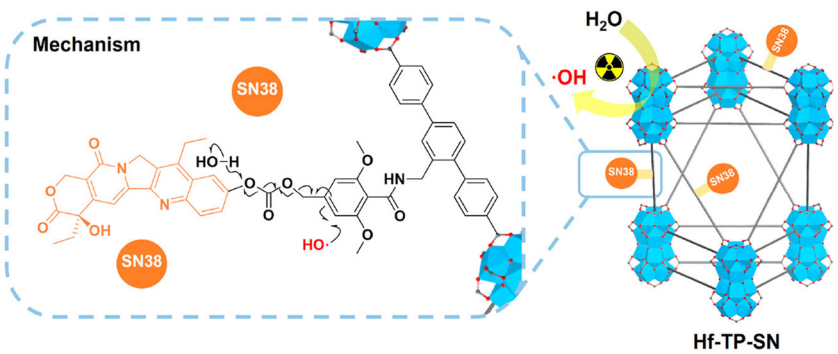

Fig. 22 Mechanism for X-ray triggered release of SN38 from Hf-TP-SN. Reprinted with permission from ref. 75. Copyright 2023, American Chemical Society.

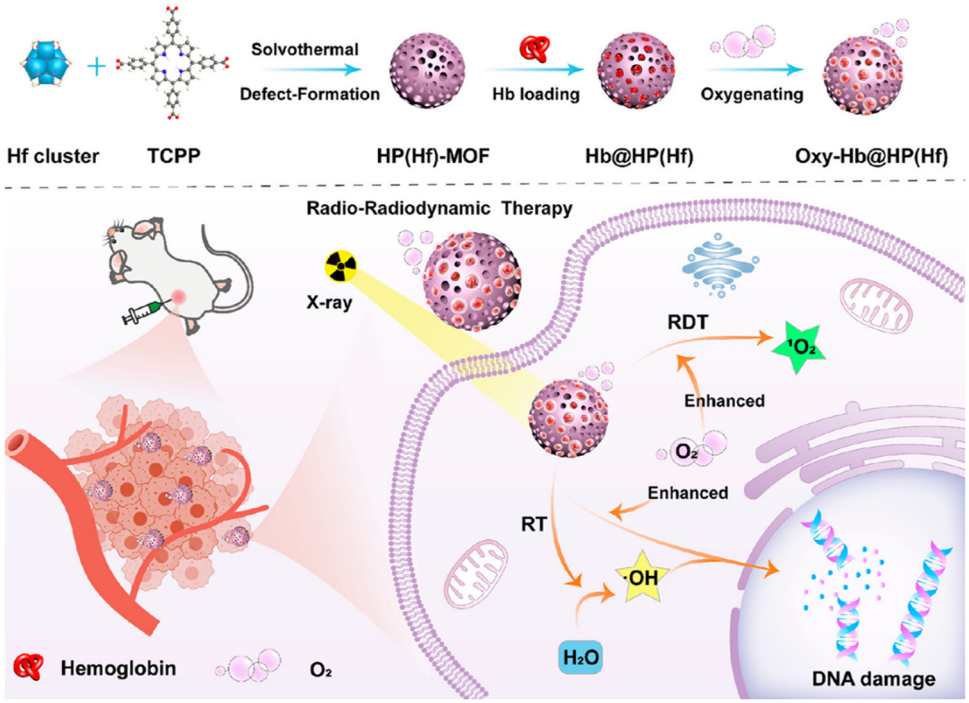

Fig. 23 Hb-Loaded Hf-MOF nanosensitizer for enhanced cancer therapy: (a) The synthesis procedure of the oxygen-rich Hb@HP(Hf) nanosensitizer and (b) Its operational mechanism within the context of radiotherapy and radioimmunotherapy for cancer treatment. Reprinted with permission from ref. 76. Copyright 2023, American Chemical Society.

enhance the formation of hydroxyl free radicals. These hydroxyl radicals can lead to the hydroxylation of 3,5-dimethoxy-benzyl carbonate and the 1,4-elimination reaction, resulting in the release of SN38 from Hf-TP-SN (Fig. 22). Its release efficiency is 6 times that of traditional small molecule prodrugs. Thus, Hf-TP-SN was able to induce significant cytotoxicity by X-ray irradiation and effectively inhibited tumor growth in mouse models of colon and breast cancer. Furthermore, Zhao *et al.* designed a MOF-based and oxygen-carrying protein based nanosensitizer Hb@HP(Hf) (Hb = hemoglobin, HP = hierarchical porous), which has the ability of radiosensitization and tumor hypoxia regulation, and can significantly enhance the anti-tumor effect of radio-radiokinetic therapy (RT-RDT) (Fig. 23).[76] This research utilizing MOFs offers a straightforward and potent approach for the development of sophisticated radiosensitizers with potential clinical relevance, offering fresh prospects for enhancing the efficacy of radiotherapy in clinical practice.

5. Summary and outlook

The high X-ray absorption capacity and tunable luminescence characteristics of MOF-based scintillators position them as promising candidate for applications in high sensitivity and high-resolution X-ray detectors, flexible imaging, and X-ray radiation therapy. In this review, we carefully reviewed the application and research progress of MOF-based scintillators in the field of X-ray fluorescence. We can conclude that significant advancements have been made in this area, including insights into the energy level transition mechanisms of fluorescence molecules, an increase in molecular structural diversity, and the development of intriguing properties and applications. However, several long-term challenges remain. Firstly, beyond the organic structural units previously mentioned, many other functional organic units can be utilized in X-ray scintillators, such as aromatic units, triphenylamine, and AIE luminogens. Selecting appropriate organic structural units is crucial for optimizing the performance of X-ray scintillators, with the goals of improving X-ray absorption efficiency, enhancing luminescent intensity, facilitating energy transfer processes, and further increasing the stability and mechanical properties in material. Secondly, the application of light metal elements in X-ray luminescence is relatively limited. Although low atomic numbers do not enhance X-ray absorption capacity, light metals can play a vital role in charge transfer between the metal center and the organic linkers, which is essential for X-ray luminescence. Furthermore, light metals can be incorporated as components in specific composites by combining them with higher-Z elements or organic ligands to create materials with tailored functions. Additionally, integrating light metals may reduce toxicity and broaden their applications in biomedicine. Thirdly, well-known strategies developed in functional materials—such as reticular chemistry, topology-guided synthesis, and post-synthetic modification—are infrequently employed to enhance the performance of MOF-based X-ray scintillators. We believe that researchers should pay more attention to these strategies for improving performance. Moreover, MOF scintillators hold

potential for improving the efficiency and resolution of gamma-ray detection due to their high-order metal nodes and adjustable optical properties. This is particularly relevant in medical imaging applications, such as gamma-ray imaging, which provide high-resolution and high-contrast imaging effects. Fourthly, regarding stability, MOF scintillators, which feature porosity and relatively weak coordination bonds, may exhibit certain limitations when compared to traditional inorganic and organic scintillators. However, the hard–soft–acid–base theory is highly instrumental in reinforcing the coordination bonds within MOFs. Moreover, ligand modification (such as the incorporation of hydrophobic groups) and wrapping with organic polymer materials to create a protective layer can significantly enhance the chemical stability of MOFs. The synergistic application of these techniques can enable MOF scintillators to perform more effectively in practical scenarios. Lastly, in addition to the structural and stability considerations mentioned above, the development of scalable manufacturing methods is crucial for their practical application. On one hand, it is essential to reduce production costs by selecting inexpensive and stable raw materials and establishing a waste recycling system to minimize resource waste and environmental pollution. Concurrently, we should opt for stable and recyclable solvents and rigorously control reaction conditions to ensure product consistency. On the other hand, shortening the production time is imperative. Typically, the production time for MOFs *via* solvothermal methods spans several days. Therefore, adopting green and efficient synthesis methods, such as microwave-assisted or continuous-flow synthesis, to reduce reaction time and enhance yield is vital. Additionally, developing automated production lines and leveraging advanced equipment to boost production efficiency and product quality are equally beneficial. Therefore, aside from enhancing performance, it is essential to consider what additional steps must be taken to meet the requirements of practical devices. We firmly believe that through collaborative efforts, MOF-based X-ray scintillator materials will demonstrate a bright future.

Data availability

No primary research results, software or code have been included and no new data were generated or analysed as part of this review.

Conflicts of interest

The authors declare that they have no known competing financial interests or personal relationships that could have appeared to influence the work reported in this paper.

Acknowledgements

This work was supported by the National Natural Science Foundation of China (Grant No. 22301135, 22171136, 22494633, and 22275084), the Natural Science Foundation of Jiangsu Province (BK20220928, BK20220079, and BK20243010), and the Fundamental Research Funds for the Central Universities (30922010301, 30921011102).

References

1 W. B. Ma, Y. R. Su, Q. S. Zhang, C. Deng, L. Pasquali, W. J. Zhu, Y. Tian, P. Ran, Z. Chen, G. Y. Yang, G. J. Liang, T. Y. Liu, H. M. Zhu, P. Huang, H. Z. Zhong, K. W. Wang, S. Q. Peng, J. L. Xia, H. F. Liu, X. Liu and Y. Yang, *Nat. Mater.*, 2022, **21**, 210.
2 C. Roques-Carmes, N. Rivera, A. Ghorashi, S. E. Kooi, Y. Yang, Z. Lin, J. Beroz, A. Massuda, J. Sloan, N. Romeo, Y. Yu, J. D. Joannopoulos, I. Kaminer, S. G. Johnson and M. Soljacic, *Science*, 2022, **375**, 837.
3 X. Y. Ou, X. Qin, B. L. Huang, J. Zan, Q. X. Wu, Z. Z. Hong, L. L. Xie, H. Y. Bian, Z. G. Yi, X. F. Chen, Y. M. Wu, X. R. Song, J. Li, Q. S. Chen, H. H. Yang and X. G. Liu, *Nature*, 2021, **590**, 20.
4 Y. Xie, G. T. Sun, J. W. Li, R. R. Sun and L. N. Sun, *J. Phys. Chem. Lett.*, 2023, **14**, 10624–10629.
5 C. Wang, O. Volotskova, K. Lu, M. Ahmad, C. Sun, L. Xing and W. Lin, *J. Am. Chem. Soc.*, 2014, **136**, 6171–6174.
6 Y. Zhang, B. Yu, Z. Zhang, X. Duan and J. Wang, *Photonics*, 2024, **11**, 803.
7 B. Q. Wang, X. Yang, S. Chen, S. R. Lu, S. Y. Zhao, Q. K. Qian, W. S. Cai, S. H. Wang and Z. G. Zang, *Iscience*, 2022, **25**, 105593.
8 F. G. Zhou, Z. Z. Li, W. Lan, Q. Wang, L. M. Ding and Z. W. Jin, *Small Methods*, 2020, **4**, 2000506.
9 X. Liu, S. Wang, W. Xie, J. Ni, K. Xiao, S. Liu, W. Lv and Q. Zhao, *J. Mater. Chem. C*, 2023, **11**, 7405–7410.
10 W. C. Röntgen, *Science*, 1896, **3**, 227–231.
11 V. I. Broser and H. Kallmann, *Z. Naturforsch.*, 1947, **2a**, 642–650.
12 C. Dujardin, E. Auffray, E. Bourret-Courchesne, P. Dorenbos, P. Lecoq, M. Nikl, A. N. Vasil'ev, A. Yoshikawa and R. Y. Zhu, *IEEE Trans. Nucl. Sci.*, 2018, **65**, 1977–1997.
13 X. Wang, H. F. Shi, H. L. Ma, W. P. Ye, L. L. Song, J. Zan, X. K. Yao, X. Y. Ou, G. H. Yang, Z. Zhao, M. Singh, C. Y. Lin, H. Wang, W. Y. Jia, Q. Wang, J. H. Zhi, C. M. Dong, X. Y. Jiang, Y. G. Tang, X. J. Xie, Y. Yang, J. P. Wang, Q. S. Chen, Y. Wang, H. H. Yang, G. Q. Zhang, Z. F. An, X. G. Liu and W. Huang, *Nat. Photonics*, 2021, **15**, 187–192.
14 F. Z. Sun, Z. Li, H. Xu, Y. Fu, H. Li, Y. Y. Yao, L. Ren, X. Q. He, Y. H. Li, R. Yang, N. Zhang, Z. G. Hu, T. Y. Ma and J. X. Zou, *Adv. Energy Mater.*, 2024, **14**, 2400875.
15 H. B. Li, Y. Lv, Z. N. Zhou, H. Tong, W. Liu and G. F. Ouyang, *Angew. Chem., Int. Ed.*, 2022, **61**, e202115225.
16 Y. W. Kang and Q. Wu, *Coord. Chem. Rev.*, 2024, **498**, 215458.
17 L. J. Xu, X. S. Lin, Q. Q. He, M. Worku and B. W. Ma, *Nat. Commun.*, 2020, **11**, 4329.
18 H. Cui, W. Zhu, Y. Deng, T. Jiang, A. Yu, H. Chen, S. Liu and Q. Zhao, *Aggregate*, 2024, **5**, e454.

19 H. Furukawa, K. E. Cordova, M. O'Keeffe and O. M. Yaghi, *Science*, 2013, **341**, 1230444.
20 J. L. Ling and C. D. Wu, *Chem. Commun.*, 2022, **58**, 8602–8613.
21 M.-H. Yu, L. Geng, Z. Chang and X.-H. Bu, *Acc. Mater. Res.*, 2023, **4**, 839–853.
22 Y. Cui, Y. Yue, G. Qian and B. Chen, *Chem. Rev.*, 2012, **112**, 1126–1162.
23 Y. Cui, J. Zhang, H. He and G. Qian, *Chem. Soc. Rev.*, 2018, **47**, 5740–5785.
24 L. Yang, P. Zhang, J. Cui, X. Cui and H. Xing, *Angew. Chem., Int. Ed.*, 2024, **63**, e202414503.
25 C. Xu, R. Fang, R. Luque, L. Chen and Y. Li, *Coord. Chem. Rev.*, 2019, **388**, 268–292.
26 T. Zhao, P. Xiao, S. Nie, M. Luo, M. Zou and Y. Chen, *Coord. Chem. Rev.*, 2024, **502**, 215592.
27 H. M. Chen, J. R. Chen, M. H. Li, M. H. You, Q. S. Chen, M. J. Lin and H. H. Yang, *Sci. China Chem.*, 2022, **65**, 2338–2350.
28 B. Chen, J. R. Wang, L. Z. Peng, Q. Wang, Y. Wang and X. W. Xu, *Adv. Funct. Mater.*, 2024, **34**, 2310270.
29 C. Vaitsis, G. Sourkouni and C. Argirusis, *Ultrason. Sonochem.*, 2019, **52**, 106–119.
30 F. J. Zheng, S. Cao, Z. L. Yang, Y. Y. Sun, Z. Z. Shen, Y. G. Wang and H. Pang, *Energy Fuels*, 2024, **38**, 11494–11520.
31 Y. Wang, X. Yin, W. Liu, J. Xie, J. Chen, M. A. Silver, D. Sheng, L. Chen, J. Diwu, N. Liu, Z. Chai, T. E. Albrecht-Schmitt and S. Wang, *Angew. Chem., Int. Ed.*, 2018, **57**, 7903.
32 H. L. Zhang, A. Li, K. Li, Z. P. Wang, X. C. Xu, Y. X. Wang, M. V. Sheridan, H. S. Hu, C. Xu, E. V. Alekseev, Z. Y. Zhang, P. Yan, K. C. Cao, Z. F. Chai, T. E. Albrecht-Schönzart and S. Wang, *Nature*, 2023, **616**, 482.
33 M. Koshimizu, *Funct. Mater. Lett.*, 2020, **13**, 2030003.
34 V. Kumar and Z. P. Luo, *Photonics*, 2021, **8**, 71.
35 Y. M. Wang, Z. R. Yang, L. H. Xiao and X. B. Yin, *Anal. Chem.*, 2018, **90**, 5758–5763.
36 Z.-R. Yang, M.-M. Wang, X.-S. Wang and X.-B. Yin, *Anal. Chem.*, 2017, **89**, 1930–1936.
37 S. Das, H. Kim and K. Kim, *J. Am. Chem. Soc.*, 2009, **131**, 3814–3815.
38 Z. Jiang, X. Xu, Y. Ma, H. S. Cho, D. Ding, C. Wang, J. Wu, P. Oleynikov, M. Jia, J. Cheng, Y. Zhou, O. Terasaki, T. Peng, L. Zan and H. Deng, *Nature*, 2020, **586**, 549–554.
39 X. Y. Li, Y. L. Zhao, S. N. Chen, K. C. Wang, S. J. Wang, L. H. Xie and J. R. Li, *Chem. Sci.*, 2024, **15**, 14425–14430.
40 C. K. Brozek and M. Dinca, *Chem. Soc. Rev.*, 2014, **43**, 5456–5467.
41 H. Y. Li, X. J. Kong, S. D. Han, J. D. Pang, T. He, G. M. Wang and X. H. Bu, *Chem. Soc. Rev.*, 2024, **53**, 5626–5676.
42 G. E. Cmarik, M. Kim, S. M. Cohen and K. S. Walton, *Langmuir*, 2012, **28**, 15606–15613.
43 N. B. Shustova, B. D. McCarthy and M. Dinca, *J. Am. Chem. Soc.*, 2011, **133**, 20126–20129.
44 P. Mondal, Z. Neuschuler, D. Mandal, R. E. Hernandez and S. M. Cohen, *Angew. Chem., Int. Ed.*, 2024, **63**, e202317062.
45 X. Y. Zhang, Z. H. Zhai, X. Q. Feng, H. W. Hou and Y. T. Zhang, *Langmuir*, 2024, **40**, 17868–17888.
46 Y. S. Bae, O. K. Farha, J. T. Hupp and R. Q. Snurr, *J. Mater. Chem.*, 2009, **19**, 2131–2134.
47 Z. Shen, W. M. Zhang, Z. Shan, S. F. Li, G. Zhang and J. Su, *Inorg. Chem.*, 2024, **63**, 8615–8624.
48 J. C. Yu, Y. J. Cui, H. Xu, Y. Yang, Z. Y. Wang, B. L. Chen and G. D. Qian, *Nat. Commun.*, 2013, **4**, 2719.
49 W. F. Wang, M. J. Xie, P. K. Wang, J. Lu, B. Y. Li, M. S. Wang, S. H. Wang, F. K. Zheng and G. C. Guo, *Angew. Chem., Int. Ed.*, 2024, **63**, e202318026.
50 B. Wang, P. Li, Y. F. Zhou, Z. L. Deng, X. P. Ouyang and Q. Xu, *ACS Appl. Nano Mater.*, 2022, **5**, 9792–9798.
51 Q. C. Peng, Y. B. Si, J. W. Yuan, Q. Yang, Z. Y. Gao, Y. Y. Liu, Z. Y. Wang, K. Li, S. Q. Zang and B. Z. Tang, *Angew. Chem., Int. Ed.*, 2023, **62**, e202308194.
52 A. V. Artem'ev, E. P. Doronina, M. I. Rakhmanova, X. Z. Hei, D. V. Stass, O. A. Tarasova, I. Y. Bagryanskaya, D. G. Samsonenko, A. S. Novikov, N. A. Nedolya and J. Li, *Dalton Trans.*, 2023, **52**, 4017–4027.
53 J. Lu, H. F. Wu, W. F. Wang, J. G. Xu, F. K. Zheng and G. C. Guo, *Chem. Commun.*, 2019, **55**, 13816–13819.
54 Q. Wang, Q. Zhou, M. Nikl, J. W. Xiao, R. Kucerkova, A. Beitlerova, V. Babin, P. Prusa, V. Linhart, J. K. Wang, X. M. Wen, G. D. Niu, J. Tang, G. H. Ren and Y. T. Wu, *Adv. Opt. Mater.*, 2022, **10**, 2200304.
55 Y. Bai, Y. B. Dou, L. H. Xie, W. Rutledge, J. R. Li and H. C. Zhou, *Chem. Soc. Rev.*, 2016, **45**, 2327–2367.
56 J. Perego, I. Villa, A. Pedrini, E. C. Padovani, R. Crapanzano, A. Vedda, C. Dujardin, C. X. Bezuidenhout, S. Bracco, P. E. Sozzani, A. Comotti, L. Gironi, M. Beretta, M. Salomoni, N. Kratochwil, S. Gundacker, E. Auffray, F. Meinardi and A. Monguzzi, *Nat. Photonics*, 2021, **15**, 393–400.
57 J. X. Wang, L. Gutiérrez-Arzaluz, X. J. Wang, M. Almalki, J. Yin, J. Czaban-Józwiak, O. Shekhah, Y. H. Zhang, O. M. Bakr, M. Eddaoudi and O. F. Mohammed, *Matter*, 2022, **5**, 253–265.
58 L. L. Zhang, X. Z. Wang, X. Wang, X. M. Wang, Y. X. Luo, C. Tan, L. S. Jiang, Y. L. Wang and W. Liu, *Inorg. Chem.*, 2023, **62**, 6421–6427.
59 P. K. Wang, W. F. Wang, B. Y. Li, M. J. Xie, H. Y. Bian, S. H. Wang, F. K. Zheng and G. C. Guo, *Inorg. Chem. Front.*, 2023, **10**, 5710–5718.
60 M. J. Xie, W. F. Wang, B. Y. Li, J. Gao, Y. F. Yan, J. Lu, F. K. Zheng and G. C. Guo, *Inorg. Chem. Commun.*, 2022, **142**, 109711.
61 W. F. Wang, J. Lu, X. M. Xu, B. Y. Li, J. Gao, M. J. Xie, S. H. Wang, F. K. Zheng and G. C. Guo, *Chem. Eng. J.*, 2022, **430**, 133010.
62 C. Wang, O. Volotskova, K. D. Lu, M. Ahmad, C. Sun, L. Xing and W. B. Lin, *J. Am. Chem. Soc.*, 2014, **136**, 6171–6174.
63 W. Zheng, H. Zhang, X. J. Wang, X. Z. Zhang, T. Long, H. Wang, W. W. Yu and C. J. Zhou, *Adv. Opt. Mater.*, 2024, **12**, 2301241.
64 J. Lu, X. H. Xin, Y. J. Lin, S. H. Wang, J. G. Xu, F. K. Zheng and G. C. Guo, *Dalton Trans.*, 2019, **48**, 1722–1731.

65 J. Lu, S. H. Wang, Y. Li, W. F. Wang, C. Sun, P. X. Li, F. K. Zheng and G. C. Guo, *Dalton Trans.*, 2020, **49**, 7309–7314.
66 C. Y. Liang, S. T. Zhang, L. W. Cheng, J. Xie, F. W. Zhai, Y. H. He, Y. X. Wang, Z. F. Chai and S. Wang, *Angew. Chem., Int. Ed.*, 2020, **59**, 11856–11860.
67 H. J. Li, Y. Li, L. Zhang, E. L. Hu, D. Zhao, H. Guo and G. D. Qian, *Adv. Mater.*, 2024, **36**, 2405535.
68 X. T. Zhang, H. Y. Qiu, W. Luo, K. F. Huang, Y. Chen, J. C. Zhang, B. H. Wang, D. L. Peng, Y. Wang and K. Z. Zheng, *Adv. Sci.*, 2023, **10**, 2207004.
69 X. M. Liu, R. H. Li, X. L. Xu, Y. Y. Jiang, W. J. Zhu, Y. Yao, F. Y. Li, X. F. Tao, S. J. Liu, W. Huang and Q. Zhao, *Adv. Mater.*, 2023, **35**, 2206741.
70 J. Lu, J. Gao, W. F. Wang, B. Y. Li, P. X. Li, F. K. Zheng and G. C. Guo, *J. Mater. Chem. C*, 2021, **9**, 5615–5620.
71 J. Lu, X. M. Jiang, J. Gao, S. H. Wang, R. X. Qian, F. K. Zheng and G. C. Guo, *Adv. Opt. Mater.*, 2024, **12**, 2302376.
72 Z. Z. Hong, Z. W. Chen, Q. S. Chen and H. H. Yang, *Acc. Chem. Res.*, 2023, **56**, 37–51.
73 L. T. Zhang, F. Gao, S. Q. Liu, M. Ju, C. Sun, G. Z. Sun, Q. Ju, K. Yang and Z. L. Fang, *Inorg. Chem. Front.*, 2024, **11**, 1607–1615.
74 C. Y. Liang, L. W. Cheng, S. T. Zhang, S. R. Yang, W. Liu, J. Xie, M. D. Li, Z. F. Chai, Y. X. Wang and S. Wang, *J. Am. Chem. Soc.*, 2022, **144**, 2189–2196.
75 Z. W. Xu, W. Y. Zhen, C. McCleary, T. K. Luo, X. M. Jiang, C. Peng, R. R. Weichselbaum and W. B. Lin, *J. Am. Chem. Soc.*, 2023, **145**, 18698–18704.
76 Y. Zhao, C. Liang, Z. J. Mei, H. X. Yang, B. Wang, C. H. Xie, Y. Xu and J. Tian, *ACS Mater. Lett.*, 2023, **5**, 3237–3247.